

Energy Variational Modeling and Numerical Simulation of Open Membranes in Stokes Flow

Han Zhou^a, Yuan-Nan Young^b and Yoichiro Mori^{a,*}

^aUniversity of Pennsylvania, Department of Mathematics, Philadelphia, PA 19104, USA

^bDepartment of Mathematical Sciences, New Jersey Institute of Technology, Newark, NJ 07102, USA

ARTICLE INFO

Keywords:

Open Lipid Bilayer Membrane
Stokes Flow
Helfrich Energy
Fluid-Structure Interaction
Boundary Integral Method

ABSTRACT

Lipid bilayer membranes are fundamental biological structures that serve as cellular boundaries, mediating transport, signaling, and maintaining structural integrity. This study introduces a novel mathematical model for open membranes immersed in Stokes flows, accounting for membrane elasticity, line tension at the open edge, and fluid-membrane interactions. The model is derived from an energy functional that incorporates Helfrich bending energy and a line energy associated with the open edge. By balancing dissipation in both the bulk fluid and the membrane surface, following the maximal dissipation principle, we derive the governing equations within an energy variational framework. Assuming axisymmetry and employing a boundary integral reduction, we transform the 3D problem into an effectively 1D problem, for which we develop a finite element-based numerical method to solve the resulting moving boundary problem. Several numerical examples are provided to validate the model and compare the results with existing studies.

1. Introduction

Lipid bilayer membranes are fundamental structural components of cellular organelles, as they self-enclose to form a vesicle in a viscous fluid to separate interior from exterior contents. As a biomimetic model for blood cells, the hydrodynamics of giant vesicles provides fundamental insights into the mechanics of biomembranes, namely the coupling between membrane and fluid mechanics [1, 2, 3, 4, 5, 6, 7]. The lipid bilayer contains a fixed number of lipid macromolecules that are free to move within the membrane. Lipid membranes can be stretched only at very high stresses, and they fail above an area strain of 4%. Accordingly the lipid bilayer is treated as an area-incompressible two-dimensional surface, displaying elastic responses under an external stress. Under normal conditions, lipid bilayer membranes close on themselves in a viscous polar solvent (such as water) to form a vesicle, characterized by its enclosed volume, surface area and bending energy [8].

Closed lipid bilayer membranes (vesicles) are modeled by the Helfrich elastic energy that accounts for a bending rigidity about $10k_B T$ ($k_B T \sim 10^{-21}$ J is the thermal energy), a spontaneous curvature, and inextensibility [9, 10, 11]. The standard Helfrich elastic membrane energy is augmented by a surface energy from the membrane tension that is not a material property but a Lagrange multiplier enforcing the local area incompressibility. The resulting fluid-structure interaction problem involves coupling the geometric PDEs for membrane shape evolution with the momentum and continuity equations for the fluid. This leads to a highly nonlinear moving boundary problem that requires robust and efficient numerical methods for accurate simulations. A variety of numerical algorithms have been developed to tackle this task, including the immersed boundary method [12, 13, 14, 15], the boundary integral method [16, 17, 18], the parametric finite element method [19], and the diffuse interface method [20, 21]. In addition, hybrid numerical methods have been developed for simulating vesicle electrohydrodynamics [22, 23].

Open lipid bilayer membranes are crucial for advancing our understanding of various biological and biophysical processes that involve opening and resealing of a lipid bilayer membrane subjected to a mechanical stress or a chemical gradient [24, 3, 25, 26]. Various techniques are developed to control the opening and closing of membranes by applying osmotic stress, using light-sensitive molecules, or employing high pulse of electric field. Electroporation, in particular, leverages the transient formation of open pores in lipid bilayers under a high electric field pulse to transport molecules, such as drugs or genetic material, across cellular membranes. These techniques enable precise manipulation of membrane opening and closing, with applications spanning from targeted drug delivery to synthetic vesicle engineering [27, 1, 28, 29].

*Corresponding author
ORCID(s):

Despite their relevance and importance, open membranes pose significant numerical challenges due to the free membrane edges. Unlike closed membranes, which are continuous and boundary-less, open membranes feature edges where the lipid bilayer tilt to avoid exposure to solvent molecules [30, 31]. These membrane edges necessitate boundary conditions that arise from local balance of forces and torques along the membrane edge [32, 28, 33]. These conditions are often expressed in terms of constraints related to line tension, bending moments, and the force balance between the membrane and the surrounding fluid. Most existing studies on open membranes focus on equilibrium configurations and rely on the Euler-Lagrange equation derived from the Helfrich energy functional [9, 34, 35, 36, 37, 38, 39, 40]. In particular, axisymmetric open lipid bilayer membranes have been extensively investigated to understand their stable equilibrium shapes, edge tension effects, and morphological transitions [41, 42, 43, 44, 45]. For open membranes with hydrodynamics, several studies have been conducted under the assumption that the membrane has a specific shape, such as a spherical cap [5, 46, 4]. Diffuse interface methods have been developed to model open membranes in the presence of hydrodynamics [47, 48] or under purely gradient flow [49]. However, these models face challenges in incorporating the local inextensibility of the membrane and accounting for surface flow. Additionally, it remains unclear what the sharp interface limit of these models is and whether they converge to it. Sharp interface descriptions of the full dynamics of open membranes with hydrodynamics remain largely unexplored, leaving a significant gap in our understanding of how open membranes evolve under external forcing and hydrodynamic interactions.

Accurate numerical simulations of open lipid bilayer membranes immersed in Stokes flow demands a robust and reliable computational framework that addresses both the geometrical complexity of the membrane and the intricate hydrodynamic interactions between the membrane and the surrounding fluid. The parametric finite element method has been successfully employed to model the dynamical evolution of open membranes by solving the gradient flow of the membrane energy. This approach, however, considers only the pure geometrical evolution of the open surface and neglects interactions with the surrounding fluid [50, 19, 51]. Numerical solutions to partial differential equations defined outside an open boundary present additional challenges due to the singular behavior near the open edge, a phenomenon referred to as the “edge condition.” [52, 53, 54] This singularity significantly complicates numerical computations. The boundary integral method has been applied to address problems such as the Laplace equation and Helmholtz equation outside open curves, offering valuable insights into handling such singularities [55, 56, 57]. Despite these advances, the numerical simulation of the Stokes flow outside an open surface, coupled with the dynamic evolution of the open surface itself, has not yet been reported in the literature.

This work develops a mathematical model and numerical framework for simulating an open axisymmetric lipid bilayer membrane immersed in an incompressible Stokesian fluid. The model is constructed from an energy-based formulation that incorporates both bending elasticity and line tension at the membrane edge. We focus on an axisymmetric reduction of the governing equations and express the solution to the Stokes equation as a boundary integral, reducing the 3D problem to a 1D problem. This approach simplifies the computational effort while preserving the essential features of the full 3D system. Based on the weak form of the reduced system, we adopted a finite element-based method combined with a semi-implicit time integration scheme to efficiently solve the time-dependent moving boundary problem. The proposed model and numerical method are validated through a series of numerical examples, with results compared against existing theoretical and numerical studies.

The remainder of this paper is organized as follows. Section 2 introduces the mathematical formulation of the model, including the membrane energy functional and the fluid–membrane interaction, which together yield the governing equations. Section 3 discusses the axisymmetric reduction and boundary integral formulation of the governing equations, reducing the problem to a 1D representation. Section 4 describes the numerical method used to solve the coupled PDE system, with particular attention to the numerical treatment of edge singularities and singular integrals. Section 5 presents our numerical experiments, along with detailed validation studies against known results, demonstrating the effectiveness of the proposed method. Finally, Section 6 concludes with a summary of the work and outlines potential directions for future research.

2. Model

This study focuses on modeling and simulating an open inextensible elastic membrane interacting with a viscous fluid in the Stokes regime (no inertial effect). In this section, we employ an energetic variational approach to derive the governing equations for the dynamics of the membrane.

2.1. Differential geometry of the open membrane

To present the governing equations, we first introduce some key differential geometric concepts for an open surface and its boundary. Consider an open inextensible, elastic membrane with one or multiple holes. The membrane is assumed to be a smooth and orientable open surface $\Gamma \subset \mathbb{R}^3$ with zero thickness (Figure 1). The boundary $\partial\Gamma$ corresponds to the open edge of elastic membrane Γ . Suppose the membrane is immersed in an incompressible viscous fluid in the domain $\Omega = \mathbb{R}^3 \setminus \bar{\Gamma}$.

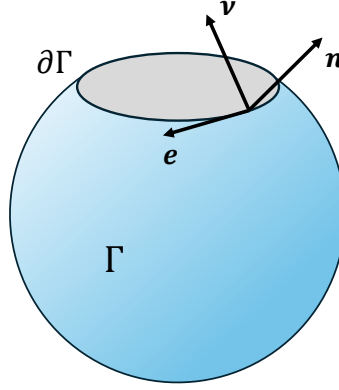


Figure 1: Illustration for an open membrane surface Γ with boundary $\partial\Gamma$. \mathbf{n} is the unit normal of Γ , \mathbf{e} is the tangent and \mathbf{v} is the co-normal along the edge $\partial\Gamma$.

Consider the surface characterized by the parametrization $\mathbf{X}(\boldsymbol{\theta}) \in \Gamma \subset \mathbb{R}^3$, where $\boldsymbol{\theta} = (\theta_1, \theta_2)$ denotes a coordinate system defined on the open set \mathcal{U} . The metric tensor is determined as

$$g_{ij} = \partial_{\theta_i} \mathbf{X} \cdot \partial_{\theta_j} \mathbf{X}, \quad \text{for } i, j = 1, 2. \quad (2.1)$$

The dual tangent vectors are given by

$$\mathbf{X}_1^* = g^{11} \partial_{\theta_1} \mathbf{X} + g^{12} \partial_{\theta_2} \mathbf{X}, \quad \mathbf{X}_2^* = g^{21} \partial_{\theta_1} \mathbf{X} + g^{22} \partial_{\theta_2} \mathbf{X}, \quad (2.2)$$

where $(g^{ij}) = (g_{ij})^{-1}$ represents the inverse of the metric tensor. Utilizing the dual tangent vectors, the surface gradient and surface divergence of a scalar function f and a vector field \mathbf{g} defined on Γ can be represented as

$$\nabla_{\Gamma} f = \frac{\partial f}{\partial \theta_1} \mathbf{X}_1^* + \frac{\partial f}{\partial \theta_2} \mathbf{X}_2^*, \quad \nabla_{\Gamma} \cdot \mathbf{g} = \frac{\partial \mathbf{g}}{\partial \theta_1} \cdot \mathbf{X}_1^* + \frac{\partial \mathbf{g}}{\partial \theta_2} \cdot \mathbf{X}_2^* \quad (2.3)$$

Define the unit normal vector field \mathbf{n} of the surface as

$$\mathbf{n} = \frac{\partial_{\theta_1} \mathbf{X} \times \partial_{\theta_2} \mathbf{X}}{|\partial_{\theta_1} \mathbf{X} \times \partial_{\theta_2} \mathbf{X}|}. \quad (2.4)$$

Defining the curvature tensor $\mathbf{L} = -\nabla_{\Gamma} \mathbf{n}$ (also referred to as the Weingarten map), the mean and Gaussian curvatures H and K can be expressed as

$$H = \frac{1}{2} \text{tr} \mathbf{L}, \quad K = \frac{1}{2} ((\text{tr} \mathbf{L})^2 - \text{tr} (\mathbf{L}^2)). \quad (2.5)$$

The orthogonal projection onto the tangent space of Γ , denoted as \mathbf{P}_{Γ} , is given by

$$\mathbf{P}_{\Gamma} = \mathbf{I} - \mathbf{n} \otimes \mathbf{n} = \nabla_{\Gamma} \mathbf{X} = \sum_i \boldsymbol{\tau}_i \otimes \boldsymbol{\tau}_i, \quad (2.6)$$

where $\boldsymbol{\tau}_i$, with $i = 1, 2$, denotes orthogonal unit tangent vectors on the surface.

In Figure 1, the unit tangent \mathbf{e} along the edge $\partial\Gamma$ is chosen such that the outward pointing unit co-normal vector \mathbf{v} of $\partial\Gamma$, given by $\mathbf{v} = \mathbf{e} \times \mathbf{n}$, is oriented away from Γ . The Darboux frame for $\partial\Gamma$ is denoted as $\{\mathbf{e}, \mathbf{n}, \mathbf{v}\}$, and it satisfies the following relationships

$$\mathbf{e}' = \kappa_n \mathbf{n} - \kappa_g \mathbf{v}, \quad \mathbf{n}' = -\kappa_n \mathbf{e} - \tau_g \mathbf{v}, \quad \mathbf{v}' = \kappa_g \mathbf{e} + \tau_g \mathbf{n}, \quad (2.7)$$

where the prime denotes the derivative with respect to the arc length parameter s of $\partial\Gamma$, κ_n and κ_g represent the normal and geodesic curvatures of $\partial\Gamma$, and τ_g stands for the geodesic torsion of $\partial\Gamma$.

2.2. Energy variational formulations

A lipid bilayer membrane in a given configuration stores free energy, which drives the system toward configurations of lower energy by generating conservative forces. For an open lipid bilayer membrane, the total free energy consists of contributions from both the curvature elasticity of the membrane surface and the line tension of the edge. Mathematically, this is expressed as

$$\mathcal{E} = \mathcal{E}_\Gamma + \mathcal{E}_{\partial\Gamma}. \quad (2.8)$$

The curvature elasticity of the membrane is modeled using the Helfrich energy, which is given by

$$\mathcal{E}_\Gamma = \int_\Gamma \left(\alpha (H - c_0)^2 + \alpha_G K \right) d\mu_\Gamma, \quad (2.9)$$

where H is the mean curvature, K is the Gaussian curvature, c_0 is the spontaneous curvature, and α and α_G are the bending rigidities associated with the mean and Gaussian curvatures, respectively. The spontaneous curvature c_0 reflects the natural geometry of the membrane due to its molecular composition or external environment. If $c_0 = 0$ and $\alpha_G = 0$, the Helfrich energy reduces to the simpler Willmore energy, which depends only on the mean curvature. For the line tension of the edge, we consider the following energy

$$\mathcal{E}_{\partial\Gamma} = \gamma \int_{\partial\Gamma} 1 ds, \quad (2.10)$$

where γ is the constant line tension, representing the energetic cost per unit length of the edge. The line tension reflects the resistance of the edge to lengthening, arising from molecular interactions at the boundary.

The conservative forces produced by the membrane can be determined by calculating the first variation of the total energy. Let's consider an arbitrary perturbation of the surface Γ in the direction of \mathbf{Y} . The first variation of the total energy can be expressed as

$$\begin{aligned} \delta_X \mathcal{E}[\mathbf{X}](\mathbf{Y}) &= \left. \frac{d}{d\varepsilon} \mathcal{E}[\mathbf{X} + \varepsilon \mathbf{Y}] \right|_{\varepsilon=0} \\ &= \int_\Gamma \alpha (\Delta_\Gamma H + 2(H - c_0)(H^2 + Hc_0 - K)) (\mathbf{n} \cdot \mathbf{Y}) d\mu_\Gamma \\ &\quad + \int_{\partial\Gamma} (\alpha(H - c_0)^2 + \alpha_G K + \gamma \kappa_g) (\mathbf{v} \cdot \mathbf{Y}) - (\alpha \nabla_\Gamma H \cdot \mathbf{v} - \alpha_G \tau_g' + \gamma \kappa_n) (\mathbf{n} \cdot \mathbf{Y}) \\ &\quad + (\alpha(H - c_0) + \alpha_G \kappa_n) \mathbf{v} \cdot \nabla_\Gamma (\mathbf{Y} \cdot \mathbf{n}) ds. \end{aligned} \quad (2.11)$$

We refer readers to [9] for a detailed derivation of the first variation of the Helfrich energy. The velocities of the bulk fluid flow and the surface flow are denoted by \mathbf{u} and \mathbf{U} , respectively. Under the assumptions of an impermeable membrane with a no-slip condition, the compatibility constraint $\mathbf{u} = \mathbf{U}$ is imposed on the surface Γ . The membrane's evolution is governed by the geometric evolution equation given by

$$\frac{\partial}{\partial t} \mathbf{X} = \mathbf{U}(\mathbf{X}) = \mathbf{u}(\mathbf{X}), \quad \mathbf{X} \in \Gamma. \quad (2.12)$$

Furthermore, it is assumed that the fluid approaches rest at infinity, adhering to the condition

$$|\mathbf{u}(\mathbf{x})| \rightarrow 0 \quad \text{as } |\mathbf{x}| \rightarrow \infty. \quad (2.13)$$

The fluid environment within cells is commonly described as a low Reynolds number flow [4, 27], typically modeled using the Stokes equation. Additionally, it has been proposed that dissipation resulting from membrane viscosity plays a crucial role for large vesicles and introduces a significant regularization effect for small pores [4, 9, 58]. We consider both the bulk viscosity and membrane viscosity in formulating the model. Let μ and μ_Γ represent the constant viscosity coefficients of the bulk fluid and the membrane, respectively. The viscous dissipation in the bulk fluid and on the membrane surface can be characterized by the Rayleigh dissipation functions defined as ,

$$\mathcal{R}[u] = \int_{\Omega} \mu \mathbf{D}(u) : \mathbf{D}(u) dx, \quad \mathcal{R}_\Gamma[U] = \int_{\Gamma} \mu_\Gamma \mathbf{D}_\Gamma(U) : \mathbf{D}_\Gamma(U) d\mu_\Gamma, \quad (2.14)$$

where $\mathbf{D}(u)$ and $\mathbf{D}_\Gamma(U)$ are the rate of deformation tensors for the bulk and surface fluid flows, defined as

$$\mathbf{D}(u) = \frac{1}{2} (\nabla u + \nabla u^\top), \quad \mathbf{D}_\Gamma(U) = \frac{1}{2} \mathbf{P}_\Gamma (\nabla_\Gamma U + \nabla_\Gamma U^\top) \mathbf{P}_\Gamma. \quad (2.15)$$

Here, \mathbf{P}_Γ is the projection operator onto the tangent plane of Γ defined in Equation (2.6). The fluid dynamics under consideration pertain to incompressible bulk Stokes flow where the bulk velocity field is divergence-free:

$$\nabla \cdot u = 0 \quad \text{in } \Omega. \quad (2.16)$$

To account for the incompressibility constraint in the bulk, we construct a Lagrangian functional related to the viscous dissipation within the bulk based on the Rayleigh dissipation function,

$$L[u, p] = \int_{\Omega} \mu \mathbf{D}(u) : \mathbf{D}(u) - p (\nabla \cdot u) dx, \quad (2.17)$$

where the pressure p in the bulk is a Lagrange multiplier for enforcing the incompressibility condition. Moreover, the assumption of local inextensibility of the lipid bilayer membrane implies

$$\nabla_\Gamma \cdot U = 0 \quad \text{on } \Gamma. \quad (2.18)$$

To address this constraint, a Lagrangian functional associated with the viscous dissipation on the membrane surface is constructed as

$$L_\Gamma[U, P] = \int_{\Gamma} \mu_\Gamma \mathbf{D}_\Gamma(U) : \mathbf{D}_\Gamma(U) - P (\nabla_\Gamma \cdot U) d\mu_\Gamma, \quad (2.19)$$

where the Lagrange multiplier P enforces area incompressibility (Equation (2.18)) and corresponds to the negative surface tension. The dissipative force can be determined by calculating the first variation of the Lagrangian functionals. Let δu and δU denote arbitrary perturbations of the bulk and surface velocities, respectively. As x tends to infinity, the perturbation decays such that $|\mathbf{v}| \rightarrow 0$ as $|x| \rightarrow \infty$. The first variations of L can be expressed as follows

$$\begin{aligned} \delta_u L[u, p](v) &= \left. \frac{d}{d\varepsilon} L[u + \varepsilon v, p] \right|_{\varepsilon=0} \\ &= \int_{\Omega} (2\mu \mathbf{D}(u) - p \mathbf{I}) : \mathbf{D}(v) dx \\ &= \int_{\Omega} (-\nabla \cdot \boldsymbol{\sigma}) v dx + \int_{\Gamma} \llbracket \boldsymbol{\sigma} n \rrbracket \cdot v d\mu_\Gamma, \end{aligned} \quad (2.20)$$

where the stress tensor $\boldsymbol{\sigma}$ is defined as $\boldsymbol{\sigma}(u, p) = -p \mathbf{I} + 2\mu \mathbf{D}(u)$, and $\llbracket \boldsymbol{\sigma} n \rrbracket$ denotes the jump of normal stress on Γ , given by

$$\llbracket \boldsymbol{\sigma} n \rrbracket(x) = \lim_{\varepsilon \rightarrow 0} (\boldsymbol{\sigma}(x - \varepsilon n(x)) - \boldsymbol{\sigma}(x + \varepsilon n(x))) n(x), \quad x \in \Gamma. \quad (2.21)$$

Similarly, the first variations of L_Γ can be expressed as

$$\begin{aligned} \delta_U L_\Gamma[U, P](V) &= \left. \frac{d}{d\varepsilon} L_\Gamma[U + \varepsilon V, P] \right|_{\varepsilon=0} \\ &= \int_{\Gamma} (2\mu_\Gamma \mathbf{D}_\Gamma(U) - P \mathbf{I}) : \mathbf{D}_\Gamma(V) d\mu_\Gamma \\ &= \int_{\Gamma} (-\nabla_\Gamma \cdot \boldsymbol{\sigma}_\Gamma) \cdot V d\mu_\Gamma + \int_{\partial\Gamma} (\boldsymbol{\sigma}_\Gamma \nu) \cdot V ds, \end{aligned} \quad (2.22)$$

where the stress tensor for membrane fluid flow σ_Γ is defined as $\sigma_\Gamma(\mathbf{U}, P) = -P\mathbf{P}_\Gamma + 2\mu_\Gamma\mathbf{D}_\Gamma(\mathbf{U})$.

2.3. Governing equations

The governing equations are derived via the principle of maximum dissipation, formulated as a variational condition on the rate of energy dissipation (see for example [59]). For our problem, this can be written as follows

$$\delta_{\mathbf{X}}\mathcal{E}[\mathbf{X}](\mathbf{Y}) = -(\delta L[\mathbf{u}, p](\mathbf{v}) + \delta L_\Gamma[\mathbf{U}, P](\mathbf{V})), \quad (2.23)$$

where the three terms above were computed in (2.11), (2.20), and (2.22) respectively. The above is to be satisfied for any arbitrary variations \mathbf{Y} , \mathbf{V} and \mathbf{v} that satisfy the kinematic constraint $\mathbf{Y} = \mathbf{V} = \mathbf{v}$ on Γ in Equation (2.12). We obtain the following governing equations for an open membrane immersed in a viscous fluid.

$$-\nabla \cdot \boldsymbol{\sigma} = \mathbf{0}, \quad \text{in } \Omega, \quad (2.24a)$$

$$-\nabla \cdot \mathbf{u} = 0, \quad \text{in } \Omega, \quad (2.24b)$$

$$-\nabla_\Gamma \cdot \boldsymbol{\sigma}_\Gamma + \llbracket \boldsymbol{\sigma} \mathbf{n} \rrbracket + \alpha (\Delta_\Gamma H + 2(H - c_0)(H^2 + Hc_0 - K)) \mathbf{n} = \mathbf{0}, \quad \text{on } \Gamma, \quad (2.24c)$$

$$-\nabla_\Gamma \cdot \mathbf{U} = \mathbf{0}, \quad \text{on } \Gamma, \quad (2.24d)$$

$$\mathbf{u} = \mathbf{U}, \quad \text{on } \Gamma, \quad (2.24e)$$

$$\partial_t \mathbf{X} = \mathbf{U}, \quad \text{on } \Gamma, \quad (2.24f)$$

$$\boldsymbol{\sigma}_\Gamma \mathbf{v} + \left(\alpha (H - c_0)^2 + \alpha_G K + \gamma \kappa_g \right) \mathbf{v} = \mathbf{0}, \quad \text{on } \partial\Gamma, \quad (2.24g)$$

$$\alpha \nabla_\Gamma H \cdot \mathbf{v} - \alpha_G \tau'_g + \gamma \kappa_n = 0, \quad \text{on } \partial\Gamma, \quad (2.24h)$$

$$\alpha (H - c_0) + \alpha_G \kappa_n = 0, \quad \text{on } \partial\Gamma. \quad (2.24i)$$

Equation (2.24c), which serves as the interfacial boundary condition for the bulk Stokes equations, states that the bulk fluid stress jump is balanced by bending forces and surface viscous forces on the membrane Γ . This is further supplemented by boundary conditions at the edge $\partial\Gamma$. Equations (2.24g) and (2.24h) express the force balance conditions in the co-normal and normal directions, respectively. Equation (2.24i) expresses the torque-free condition at $\partial\Gamma$. Our derivation ensures that in the above system the rate of change in energy is balanced by energy dissipation. Indeed, it can be shown that the above equations yield the following identity

$$\frac{d}{dt} \mathcal{E} = -2 \int_\Omega \mu |\mathbf{D}(\mathbf{u})|^2 d\mathbf{x} - 2 \int_\Gamma \mu_\Gamma |\mathbf{D}_\Gamma(\mathbf{U})|^2 d\mu_\Gamma. \quad (2.25)$$

where $|\mathbf{D}(\mathbf{u})|$ and $|\mathbf{D}_\Gamma(\mathbf{U})|$ are the Frobenius norms of the deformation tensors.

2.4. Boundary integral and weak form

The governing equations for an open membrane in Stokes flow involve coupling the surface evolution equations with the bulk Stokes equation. Given the complex surface geometry, directly solving these equations using both bulk and surface meshes necessitates sophisticated handling of the boundary conditions on the surface. To address these challenges, we employ boundary integral formulations for the bulk Stokes equation, reducing the bulk-surface coupled PDE system to a set of differential-integral equations confined to the surface.

Since the velocity field is expected to be continuous on the surface while the stress exhibits discontinuity, it is natural and common to adopt a single-layer representation for the solution of the bulk Stokes equation. It is worth noting that for problems involving an open edge, a double-layer representation of the solution is unsuitable. This is because a double-layer potential becomes multi-valued at the open edge if the function's jump is non-zero at that location. Let $G(\mathbf{x})$ be the Stokeslet in 3D free spaces, whose entries are given by

$$G_{ij}(\mathbf{x}) = -\frac{1}{8\pi} \left(\frac{\delta_{ij}}{|\mathbf{x}|} + \frac{x_i x_j}{|\mathbf{x}|^3} \right). \quad (2.26)$$

For a surface density function \mathbf{f} , define the single-layer integral operator S as

$$(S[\mathbf{f}])_i(\mathbf{x}) = -\frac{1}{\mu} \int_\Gamma G_{ij}(\mathbf{x} - \mathbf{x}') f_j(\mathbf{x}') d\mu(\mathbf{x}'), \quad \mathbf{x} \in \mathbb{R}^3, \quad (2.27)$$

where we have followed the Einstein summation convention. Using the Stokeslet, the velocity field of the fluid flow can be expressed as a single-layer boundary integral

$$\mathbf{u}(\mathbf{x}) = S[\xi](\mathbf{x}), \quad \mathbf{x} \in \mathbb{R}^3, \quad (2.28)$$

where ξ represents an unknown single-layer density, introduced as an auxiliary variable. Observing the relation $\xi = \llbracket \sigma \mathbf{n} \rrbracket$, this provides an additional justification for choosing the single-layer representation. The auxiliary variable ξ has a clear physical interpretation as the exerted force, which can be directly used to enforce the force balance on Γ in equation (2.24c). The single-layer integral is continuous across the surface and its restriction on Γ is well-defined, which we also denote by $S[\xi]$. Thus, we have $\mathbf{U} = S[\xi]$ on Γ .

Due to the bending force, which introduces the surface Laplacian of the mean curvature, the original equations (2.24) are high-order in space. Numerical approximation for such high-order PDEs is challenging and typically requires high-order basis functions, adding complexity. To simplify, we treat the mean curvature H as an unknown function and reformulate the equations in a mixed form. Additionally, we introduce auxiliary variables, including the mean curvature vector \mathbf{H} and the normal bending force g . Then we reformulate the problem as finding $\xi, \mathbf{U}, P, \mathbf{X}, \mathbf{H}, H, g$ such that the following equations are satisfied

$$-S[\xi] + \mathbf{U} = \mathbf{0}, \quad \text{on } \Gamma, \quad (2.29a)$$

$$\xi - \nabla_\Gamma \cdot \sigma_\Gamma + g \mathbf{n} = \mathbf{0}, \quad \text{on } \Gamma, \quad (2.29b)$$

$$-\nabla_\Gamma \cdot \mathbf{U} = \mathbf{0}, \quad \text{on } \Gamma, \quad (2.29c)$$

$$\partial_t \mathbf{X} = \mathbf{U}, \quad \text{on } \Gamma, \quad (2.29d)$$

$$2\mathbf{H} - \Delta_\Gamma \mathbf{X} = \mathbf{0}, \quad \text{on } \Gamma, \quad (2.29e)$$

$$\mathbf{H} - \mathbf{n} \cdot \mathbf{H} = 0, \quad \text{on } \Gamma, \quad (2.29f)$$

$$g - \alpha (\Delta_\Gamma H + 2(H - c_0)(H^2 + Hc_0 - K)) = 0, \quad \text{on } \Gamma, \quad (2.29g)$$

together with boundary conditions (2.24g), (2.24h), and (2.24i).

Beginning with the mixed form, we reformulate the equations into a weak form that involves only low-order spatial derivatives. The only time derivative that appears in the geometric evolution equation, $\partial_t \mathbf{X} = \mathbf{U}$. At each fixed time, we treat all quantities as functions defined on the current surface, with the equations represented as partial differential equations on the surface. Given two functions f and g defined on Γ , we define the L^2 inner product on Γ as

$$\langle f, g \rangle_\Gamma = \int_\Gamma f(\mathbf{x}) g(\mathbf{x}) d\mu_\Gamma. \quad (2.30)$$

We define the following Sobolev spaces on Γ

$$L^2(\Gamma) = \left\{ f : \int_\Gamma f^2(\mathbf{x}) d\mu_\Gamma < +\infty \right\}, \quad (2.31)$$

$$H^1(\Gamma) = \{ f \in L^2(\Gamma), \nabla_\Gamma f \in [L^2(\Gamma)]^3 \}. \quad (2.32)$$

Define the solution spaces for the mean curvature as

$$H \in H_g^1(\Gamma) = \left\{ H \in H^1(\Gamma) : H|_{\partial\Gamma} = -\frac{\alpha_G}{\alpha} \kappa_n + c_0 \right\}. \quad (2.33)$$

Note that H_g^1 is an affine space that is defined by shifting the space $H_0^1(\Gamma)$. Let $H^{-1/2}(\Gamma)$ be the dual space of the trace space $H^{1/2}(\Gamma) = \{u|_\Gamma, u \in H^1(\Omega)\}$. The weak form of (2.29) is given as follows: given the surface Γ , we find

$$\xi \in [H^{-\frac{1}{2}}(\Gamma)]^3, \quad \mathbf{H} \in [L^2(\Gamma)]^3, \quad \partial_t \mathbf{X}, \mathbf{U}, \mathbf{X} \in [H^1(\Gamma)]^3, \quad P, g \in L^2(\Gamma), \quad H \in H_g^1(\Gamma). \quad (2.34)$$

such that

$$\begin{aligned} \langle \boldsymbol{\varphi}, -S[\xi] + \mathbf{U} \rangle_\Gamma &= 0, \quad \forall \boldsymbol{\varphi} \in [L^2(\Gamma)]^3, \\ \langle \boldsymbol{\psi}, \xi \rangle_\Gamma + 2\mu_\Gamma \langle \mathbf{D}_\Gamma(\boldsymbol{\psi}), \mathbf{D}_\Gamma(\mathbf{U}) \rangle_\Gamma - \langle \nabla_\Gamma \cdot \boldsymbol{\psi}, P \rangle_\Gamma + \langle \boldsymbol{\psi}, g \mathbf{n} \rangle_\Gamma \end{aligned} \quad (2.35a)$$

$$= - \left\langle \boldsymbol{\psi}, \left(\alpha (H - c_0)^2 + \alpha_G K + \gamma \kappa_g \right) \boldsymbol{\nu} \right\rangle_{\partial\Gamma}, \quad \forall \boldsymbol{\psi} \in [H^1(\Gamma)]^3, \quad (2.35b)$$

$$- \langle Q, \nabla_\Gamma \cdot \mathbf{U} \rangle_\Gamma = 0, \quad \forall Q \in L^2(\Gamma), \quad (2.35c)$$

$$\langle \boldsymbol{\omega}, \partial_t \mathbf{X} - \mathbf{U} \rangle_\Gamma = 0, \quad \forall \boldsymbol{\omega} \in [L^2(\Gamma)]^3, \quad (2.35d)$$

$$2 \langle \boldsymbol{\zeta}, \mathbf{H} \rangle_\Gamma + \langle \nabla_\Gamma \boldsymbol{\zeta}, \nabla_\Gamma \mathbf{X} \rangle_\Gamma = \langle \boldsymbol{\zeta}, \boldsymbol{\nu} \rangle_{\partial\Gamma}, \quad \forall \boldsymbol{\zeta} \in [H^1(\Gamma)]^3, \quad (2.35e)$$

$$\langle \eta, H - \mathbf{n} \cdot \mathbf{H} \rangle_\Gamma = 0, \quad \forall \eta \in H_0^1(\Gamma), \quad (2.35f)$$

$$\begin{aligned} & \langle \chi, g \rangle_\Gamma + \alpha \langle \nabla_\Gamma \chi, \nabla_\Gamma \mathbf{H} \rangle_\Gamma - 2\alpha \langle \chi, (H - c_0) (H^2 + Hc_0 - K) \rangle_\Gamma \\ & = \left\langle \chi, \alpha_G \tau'_g - \gamma \kappa_n \right\rangle_{\partial\Gamma}, \quad \forall \chi \in H^1(\Gamma). \end{aligned} \quad (2.35g)$$

In this formulation, \mathbf{X} effectively serves as the identity mapping on Γ , and its time derivative $\partial_t \mathbf{X}$ should be interpreted as the velocity of the boundary points on Γ at the current time. Note that we have used a boundary condition $\nabla_\Gamma \mathbf{X} \cdot \boldsymbol{\nu} = \boldsymbol{\nu}$ in (2.35e), which is defined implicitly due to geometric consistency.

It is important to note that, since the surface is open, the single-layer density $\boldsymbol{\xi}$ exhibits a singular behavior like $d^{-1/2}$, where d is the Euclidean distance to the open edge, even when the surface Γ and velocity \mathbf{U} are smooth. This is known as the "edge condition." Such an edge singularity means that $\boldsymbol{\xi}$ is no longer in $L^2(\Gamma)$ but only in $H^{-1/2}(\Gamma)$ for $\mathbf{U} \in H^1(\Gamma) \subset H^{1/2}(\Gamma)$ [54, 52, 53].

3. Axisymmetric formulations

To reduce computational complexity and enable more efficient numerical simulation, we simplify the governing equation (2.24) and its weak form equation (2.35), originally formulated for open surfaces, by restricting to the axisymmetric case. While the full 3D formulation remains applicable to arbitrary geometries, it is computationally intensive. The axisymmetric reduction transforms the surface-based 3D problem into a lower-dimensional formulation on an open generating curve, effectively yielding a 1D problem. This simplification assumes that the membrane surface is rotationally symmetric about the z -axis and that the surrounding fluid flow is axisymmetric, with no azimuthal velocity component. As a result, the fluid velocity in the r - and z -directions, along with the pressure, are taken to be independent of the azimuthal angle φ .

Define the coordinates vectors in cylindrical coordinates by

$$\mathbf{e}_r = \begin{pmatrix} \cos \varphi \\ \sin \varphi \\ 0 \end{pmatrix}, \quad \mathbf{e}_\varphi = \begin{pmatrix} -\sin \varphi \\ \cos \varphi \\ 0 \end{pmatrix}, \quad \mathbf{e}_z = \begin{pmatrix} 0 \\ 0 \\ 1 \end{pmatrix}. \quad (3.1)$$

Let the surface Γ be generated by the rotation of a planar curve $C : (X^r(s), X^z(s))^\top$, where $s \in \mathbb{T} = (0, L)$ denotes the arc-length parameter along the curve, around the z -axis. The resulting axisymmetric surface Γ is parameterized as

$$\Gamma : \mathbf{X}(s, \varphi) = X^r(s) \mathbf{e}_r + X^z(s) \mathbf{e}_z = \begin{pmatrix} X^r(s) \cos \varphi \\ X^r(s) \sin \varphi \\ X^z(s) \end{pmatrix}, \quad s \in \mathbb{T}, \quad \varphi \in \mathbb{S}^1 = \mathbb{R} \setminus (2\pi\mathbb{Z}). \quad (3.2)$$

Since the surface is open, the generating curve C may terminate away from the z -axis. We denote the endpoint lying on the z -axis by $\partial_0 C$, and the open edge by $\partial_1 C$. Under the axisymmetric parametrization, scalar and vector-valued functions defined on Γ can be expressed in terms of the arc-length parameter s and azimuthal angle φ . Specifically, for a scalar field f and a vector field \mathbf{f} defined on the surface, we write

$$f(\mathbf{X}(s, \varphi)) = \tilde{f}(s, \varphi), \quad \mathbf{f}(\mathbf{X}(s, \varphi)) = f^r(s, \varphi) \mathbf{e}_r + f^\varphi(s, \varphi) \mathbf{e}_\varphi + f^z(s, \varphi) \mathbf{e}_z. \quad (3.3)$$

If the fields are axisymmetric, then $\tilde{f}, f^r, f^\varphi, f^z$ are independent of the azimuthal angle φ and the functions reduce to one-dimensional representations $\tilde{f}(s), f^r(s), f^\varphi(s), f^z(s)$. In particular, under the axisymmetric assumption, there is no φ component for the functions $\mathbf{U}, \boldsymbol{\xi}$, and \mathbf{H} are assumed to have no azimuthal components, and their radial and axial components depend solely on s .

For vector fields with no azimuthal component, i.e., $f^\varphi = 0$, we introduce the reduced function $\tilde{\mathbf{f}}(s) = (f^r(s), f^z(s))^\top$. For notational simplicity, and with a slight abuse of notation, we omit the tilde and continue to denote

reduced functions using the original symbol. For instance, the generating curve is written as $\mathbf{X}(s) = (X^r(s), X^z(s))^\top$, and an axisymmetric scalar function \tilde{f} is denoted as f .

3.1. Differential operators on the axisymmetric surface

In order to reduce the fully 3D weak form (2.35) to the axisymmetric case, we write geometric quantities and differential operators on Γ using the coordinate vectors (3.1). The normal vector to the axisymmetric surface is given by

$$\mathbf{n} = -X_s^z \mathbf{e}_r + X_s^r \mathbf{e}_z. \quad (3.4)$$

The mean and Gaussian curvatures are given by, respectively,

$$H = \frac{1}{2} \left(X_s^r X_{ss}^z - X_s^z X_{ss}^r + \frac{X_s^z}{X^r} \right), \quad K = \frac{X_s^z}{X^r} (X_s^r X_{ss}^z - X_s^z X_{ss}^r). \quad (3.5)$$

Note that the current configuration allows the surface to have up to two holes, which correspond to cases where both endpoints of the generating curve C do not intersect the z -axis. For such cases, we provide the expressions for the co-normal vector and curvatures on the boundary $\partial\Gamma$. The co-normal vector to $\partial\Gamma$ is given by

$$\mathbf{v} = \begin{cases} X_s^r(L) \mathbf{e}_r + X_s^z(L) \mathbf{e}_z, & s = L, \\ -X_s^r(0) \mathbf{e}_r - X_s^z(0) \mathbf{e}_z, & s = 0. \end{cases} \quad (3.6)$$

The normal and geodesic curvatures of $\partial\Gamma$ are given by, respectively,

$$\kappa_n = \begin{cases} \left. \frac{X_s^z}{X^r} \right|_{s=L}, & s = L, \\ -\left. \frac{X_s^z}{X^r} \right|_{s=0}, & s = 0. \end{cases}, \quad \kappa_g = \begin{cases} \left. \frac{X_s^r}{X^r} \right|_{s=L}, & s = L, \\ -\left. \frac{X_s^r}{X^r} \right|_{s=0}, & s = 0. \end{cases} \quad (3.7)$$

Since the surface is axisymmetric, the torsion vanishes, i.e., $\tau_g = 0$.

For any scalar function f and vector-valued function \mathbf{f} defined on the axisymmetric surface Γ , the surface gradient and surface divergence simplify to the following forms

$$\nabla_\Gamma f = f_s (X_s^r \mathbf{e}_r + X_s^z \mathbf{e}_z) + \frac{f_\varphi}{X^r} \mathbf{e}_\varphi, \quad (3.8)$$

$$\nabla_\Gamma \cdot \mathbf{f} = f_s^r X_s^r + f_s^z X_s^z + \frac{f^r + f_\varphi^\varphi}{X^r}, \quad (3.9)$$

where subscripts s and φ denote partial derivatives with respect to the surface and azimuthal coordinates, respectively. Furthermore, let \mathbf{f} and \mathbf{g} be vector-valued axisymmetric functions in the following form

$$\mathbf{f}(s, \varphi) = f^r(s) \mathbf{e}_r + f^z(s) \mathbf{e}_z, \quad \mathbf{g}(s, \varphi) = g^r(s) \mathbf{e}_r + g^z(s) \mathbf{e}_z, \quad (3.10)$$

Utilizing (3.8), the surface gradient and deformation tensor of \mathbf{f} are given by

$$\nabla_\Gamma \mathbf{f} = (f_s^r \mathbf{e}_r + f_s^z \mathbf{e}_z) \otimes (X_s^r \mathbf{e}_r + X_s^z \mathbf{e}_z) + \frac{f^r}{X^r} \mathbf{e}_\varphi \otimes \mathbf{e}_\varphi, \quad (3.11)$$

$$\mathbf{D}_\Gamma(\mathbf{f}) = (\mathbf{X}_s \cdot \mathbf{f}_s) (X_s^r \mathbf{e}_r + X_s^z \mathbf{e}_z) \otimes (X_s^r \mathbf{e}_r + X_s^z \mathbf{e}_z) + \frac{f^r}{X^r} \mathbf{e}_\varphi \otimes \mathbf{e}_\varphi. \quad (3.12)$$

The double dot product for surface gradient of vector-valued functions and deformation tensors are computed as follows.

$$\nabla_\Gamma \mathbf{f} : \nabla_\Gamma \mathbf{g} = \mathbf{f}_s \cdot \mathbf{g}_s + \frac{f^r g^r}{(X^r)^2}, \quad (3.13)$$

$$\nabla_\Gamma \mathbf{f} : \mathbf{D}_\Gamma(\mathbf{g}) = (\mathbf{X}_s \cdot \mathbf{g}_s) (\mathbf{X}_s \cdot \mathbf{f}_s) + \frac{f^r g^r}{(X^r)^2}, \quad (3.14)$$

$$\mathbf{D}_\Gamma(\mathbf{f}) : \mathbf{D}_\Gamma(\mathbf{g}) = (\mathbf{X}_s \cdot \mathbf{g}_s) (\mathbf{X}_s \cdot \mathbf{f}_s) + \frac{f^r g^r}{(X^r)^2}. \quad (3.15)$$

By substituting the variables in the weak form (2.35) with their axisymmetric expressions, we derive the weak form of the governing equations (2.24) under the axisymmetric assumption, which is summarized in (3.34).

3.2. Axisymmetric single-layer integral

For the single-layer integral $S[\xi]$, by the axisymmetric assumption, we integrate the φ variable to obtain an explicit formula for the axisymmetric single-layer integral,

$$S[\xi](\mathbf{X}(s, \varphi)) = -\frac{1}{\mu} \int_{\mathbb{T}} \int_{\mathbb{S}^1} G(\mathbf{X}(s, \varphi) - \mathbf{X}(s', \varphi')) \xi(\mathbf{X}(s', \varphi')) X^r(s') d\varphi' ds' = (S[\xi])^r e_r + (S[\xi])^z e_z, \quad (3.16)$$

where both $(S[\xi])^r$ and $(S[\xi])^z$ are independent of φ . By extracting r - and z -direction component of $S[\xi]$, we can now express the velocity using the axisymmetric single-layer integral

$$\mathbf{U}(s) = \begin{pmatrix} (S[\xi])^r \\ (S[\xi])^z \end{pmatrix} (s) = \frac{1}{8\pi\mu} \int_{\mathbb{T}} X^r(s') \mathcal{S}(s, s') \xi(s') ds' \stackrel{\text{def}}{=} S[\xi](s), \quad s \in \mathbb{T}, \quad (3.17)$$

where the kernel function $\mathcal{S}(s, s')$ is given by

$$\mathcal{S}(s, s') = \begin{pmatrix} I_{11} + (r^2 + (r')^2)I_{31} - rr'(I_{30} + I_{32}) & \Delta z(rI_{30} - r'I_{31}) \\ \Delta z(rI_{31} - r'I_{30}) & I_{10} + (\Delta z)^2 I_{30} \end{pmatrix}, \quad (3.18)$$

with $r = X^r(s)$, $r' = X^r(s')$, $\Delta z = X^z(s) - X^z(s')$. Here, $I_{mn} = I_{mn}(r, r', \Delta z)$ is related to complete elliptic integrals,

$$I_{mn}(r_1, r_2, \hat{z}) = \frac{2}{((r_1 - r_2)^2 + \hat{z}^2)^{\frac{m}{2}}} I_{mn}^{(1)}(k_1) + \frac{2}{((r_1 + r_2)^2 + \hat{z}^2)^{\frac{m}{2}}} I_{mn}^{(2)}(k_2), \quad (3.19)$$

where

$$I_{mn}^{(1)}(k_1) = \int_0^{\frac{\pi}{2}} \frac{(1 - 2 \sin^2 \theta')^n}{(1 + k_1^2 \sin^2 \theta')^{\frac{m}{2}}} d\theta', \quad k_1^2 = \frac{4r_1 r_2}{(r_1 - r_2)^2 + \hat{z}^2}, \quad (3.20)$$

$$I_{mn}^{(2)}(k_2) = \int_0^{\frac{\pi}{2}} \frac{(2 \sin^2 \theta' - 1)^n}{(1 - k_2^2 \sin^2 \theta')^{\frac{m}{2}}} d\theta', \quad k_2^2 = \frac{4r_1 r_2}{(r_1 + r_2)^2 + \hat{z}^2} \in [0, 1). \quad (3.21)$$

and

$$I_{mn}^{(1)}(k) = \frac{1}{(1 + k^2)^{\frac{m}{2}}} I_{mn}^{(2)}\left(\sqrt{\frac{k^2}{1 + k^2}}\right). \quad (3.22)$$

Let $K(k)$, $E(k)$ be complete elliptic integrals of the first and second kind. The terms $I_{mn}^{(1)}(k)$ and $I_{mn}^{(2)}(k)$ can be written as linear combinations of $K(k)$ and $E(k)$. In particular, for $m = 1$, we have

$$I_{10}^{(2)}(k) = K(k), \quad I_{11}^{(2)}(k) = \frac{2}{k^2}(K(k) - E(k)) - K(k), \quad (3.23)$$

and, for $m = 3$, we have

$$I_{30}^{(2)}(k) = \frac{1}{1 - k^2} E(k), \quad (3.24)$$

$$I_{31}^{(2)}(k) = \frac{2}{k^2} \left(\frac{1}{1 - k^2} E(k) - K(k) \right) - \frac{1}{1 - k^2} E(k), \quad (3.25)$$

$$I_{32}^{(2)}(k) = \frac{4}{k^4} \left(\frac{2 - k^2}{1 - k^2} E(k) - 2K(k) \right) - \frac{4}{k^2} \left(\frac{1}{1 - k^2} E(k) - K(k) \right) + \frac{1}{1 - k^2} E(k). \quad (3.26)$$

3.3. Axisymmetric formulation of the governing equations

Combining the results from the previous two subsections, we can now formulate the weak form for the axisymmetric case of (2.24). The L^2 inner-product on Γ naturally defines the weighted L^2 inner-product on the generating curve \mathcal{C} ,

$$\int_{\Gamma} f(\mathbf{x}) g(\mathbf{x}) d\mu_{\Gamma} = 2\pi \int_{\mathbb{T}} X^r(s) f(s) g(s) ds \stackrel{\text{def}}{=} 2\pi \langle f, g \rangle_{\mathcal{C}}. \quad (3.27)$$

We define the weighted Sobolev spaces on C

$$L^2(C) = \{f : \langle f, f \rangle_C < +\infty\}. \quad (3.28)$$

$$H^1(C) = \{f \in L^2(C), \partial_s f \in L^2(C)\}. \quad (3.29)$$

Similarly, define the solution space for mean curvature,

$$H \in H_g^1(C) = \left\{ H \in H^1(C) : H|_{\partial C} = -\frac{\alpha_G}{\alpha} \kappa_n + c_0 \right\}. \quad (3.30)$$

Moreover, we define the following functional spaces

$$H_0^1(C) = \{f \in H^1(C) : f^r(s) = 0, \quad \forall s \text{ such that } \mathbf{X}(s) \in \partial_1 C\}, \quad (3.31)$$

$$V_\partial(C) = \{f \in [H^1(C)]^2 : f^r(s) = 0, \quad \forall s \text{ such that } \mathbf{X}(s) \in \partial_0 C\}. \quad (3.32)$$

The weak form for the axisymmetric case is as follows: given the generating curve C of the membrane surface, we find

$$\xi \in [H^{-\frac{1}{2}}(C)]^2, \quad \mathbf{H} \in [L^2(C)]^2, \quad \partial_t \mathbf{X}, \mathbf{U}, \mathbf{X} \in V_\partial(C), \quad P, g \in L^2(C), \quad H \in H_g^1(C). \quad (3.33)$$

such that

$$\langle \boldsymbol{\varphi}, -S[\xi] + \mathbf{U} \rangle_C = 0, \quad \forall \boldsymbol{\varphi} \in [L^2(C)]^2, \quad (3.34a)$$

$$\begin{aligned} & \langle \boldsymbol{\psi}, \xi \rangle_C + 2\mu_\Gamma \langle \mathbf{X}_s \cdot \boldsymbol{\psi}_s, \mathbf{X}_s \cdot \mathbf{U}_s \rangle_C + 2\mu_\Gamma \left\langle \frac{\boldsymbol{\psi}^r}{X^r}, \frac{U^r}{X^r} \right\rangle_C - \left\langle \mathbf{X}_s \cdot \boldsymbol{\psi}_s + \frac{\boldsymbol{\psi}^r}{X^r}, P \right\rangle_C + \langle \boldsymbol{\psi}, g \mathbf{n} \rangle_C, \\ & = - \left\langle \boldsymbol{\psi}, \left(\alpha (H - c_0)^2 + \alpha_G K + \gamma \kappa_g \right) \mathbf{v} \right\rangle_{\partial C}, \quad \forall \boldsymbol{\psi} \in V_\partial(C), \end{aligned} \quad (3.34b)$$

$$- \left\langle Q, \mathbf{X}_s \cdot \mathbf{U}_s + \frac{U^r}{X^r} \right\rangle_C = 0, \quad \forall Q \in L^2(C), \quad (3.34c)$$

$$\langle \boldsymbol{\omega}, \partial_t \mathbf{X} - \mathbf{U} \rangle_C = 0, \quad \forall \boldsymbol{\omega} \in [L^2(C)]^2, \quad (3.34d)$$

$$2 \langle \zeta, \mathbf{H} \rangle_C + \langle \zeta_s, \mathbf{X}_s \rangle_C + \left\langle \frac{\zeta^r}{X^r}, \frac{X^r}{X^r} \right\rangle_C = \langle \zeta, \mathbf{v} \rangle_{\partial C}, \quad \forall \zeta \in V_\partial(C), \quad (3.34e)$$

$$\langle \eta, H - \mathbf{n} \cdot \mathbf{H} \rangle_C = 0, \quad \eta \in H_0^1(C), \quad (3.34f)$$

$$\begin{aligned} & \langle \chi, g \rangle_C + \alpha \langle \chi_s, H_s \rangle_C - 2\alpha \langle \chi, (H - c_0) (H^2 + H c_0 - K) \rangle_C \\ & = \left\langle \chi, \alpha_G \tau'_g - \gamma \kappa_n \right\rangle_{\partial C}, \quad \forall \chi \in H^1(C). \end{aligned} \quad (3.34g)$$

4. Numerical method

4.1. Finite element approximation

We approximate the weak formulation (3.34) for the curve evolution using the finite element method. The time interval $[0, T]$ is divided into a temporal mesh. For simplicity, we adopt uniform time stepping $t^n = n\Delta t$ for $n = 0, 1, 2, \dots, N_t$ with $T = N_t \Delta t$.

Note that even for the inextensible membrane surface, the arc-length parameter s of the time-dependent generating curve $C(t)$ changes during its evolution. Given a function $\Phi(\alpha)$ for $\alpha \in \mathbb{I} = (0, 1)$ with $\Phi'(\alpha) > 0$, we reparameterize the curve by $s = \Phi(\alpha)$ where α is the new parameter defined on a fixed reference domain \mathbb{I} . Denote by $(\Phi^* f)(\alpha, t) = f(\Phi(\alpha), t)$ the pullback of f to the reference domain \mathbb{I} . The curve is now represented by the function $(\Phi^* \mathbf{X})(\alpha, t), \alpha \in \mathbb{I}$. With the pullback, we are able to approximate functions defined on the curve in (3.34) by directly approximating their pullback functions on a fixed reference domain. Note that α is no longer the arc-length parameter and we have $\partial_\alpha \Phi = |\partial_\alpha(\Phi^* \mathbf{X})|$. The derivative of f with respect to the arc-length parameter s can be expressed as $\Phi^*(\partial_s f) = |\partial_\alpha(\Phi^* \mathbf{X})|^{-1} \partial_\alpha(\Phi^* f)$. The inner product $\langle \cdot, \cdot \rangle_C$ under the pullback is given by

$$\langle f, g \rangle_C = \int_{\mathbb{I}} (\Phi^* f)(\alpha) (\Phi^* g)(\alpha) (\Phi^* X^r)(\alpha) |\partial_\alpha(\Phi^* \mathbf{X})(\alpha)| d\alpha. \quad (4.1)$$

To simplify notation in further derivations, we will omit the pullback notation Φ^* and use the same symbol for a function and its pullback.

The reference domain \mathbb{I} is discretized uniformly into a uniform mesh with N smaller intervals with size $h = 1/N$, to get the nodes $\alpha_i = ih$, for $i = 0, 1, \dots, N$. With this uniform partition, we define a one-dimensional continuous piecewise polynomial finite element space as

$$V_k^N(\mathbb{I}) = \left\{ v \in C(\bar{\mathbb{I}}) : v|_{[\alpha_{i-1}, \alpha_i]} \in \mathbb{P}_k([\alpha_{i-1}, \alpha_i]), 1 \leq i \leq N \right\} \quad (4.2)$$

$$= \text{span} \left\{ \phi_k^1(x), \phi_k^2(x), \dots, \phi_k^{M_k}(x) \right\}, \quad (4.3)$$

where $\mathbb{P}_k(\mathbb{I})$ is the functional space of polynomials of degree no greater than k . Let $\{\mathbf{X}^n\}_{0 \leq i \leq N_t}$ be an numerical approximation to $\{(\Phi^* \mathbf{X})(t)\}_{t \in [0, T]}$ with $\mathbf{X}^n \in [V_2^N(\mathbb{I})]^2 \cap V_\partial(\mathbb{I})$. The curve C^n is defined as $\mathbf{X}^n(\bar{\mathbb{I}})$ and geometric quantities such as the normal vector can be computed using \mathbf{X}^n . We use quadratic elements for the surface velocity \mathbf{U} and linear elements for the surface tension P . This choice of finite element spaces mimics the Taylor-Hood element, which guarantees the inf-sup stability condition for Stokes equations on planar domains. For other quantities, we adopt quadratic element spaces for their approximations. Denote by $\xi^n, \mathbf{U}^n, P^n, \mathbf{X}^n, \mathbf{H}^n, H^n, g^n$ the numerical approximations to the pullbacks of $\xi, \mathbf{U}, P, \mathbf{X}, \mathbf{H}, H, g$ at $t = t^n$, respectively. Given an initial curve $C(0)$, its numerical approximation \mathbf{X}^0 is obtained by interpolation. For $n \geq 0$, we find

$$\mathbf{H}^{n+1}, \xi^{n+1} \in [V_2^N(\mathbb{I})]^2, \quad \mathbf{U}^{n+1}, \mathbf{X}^{n+1} \in [V_2^N(\mathbb{I})]^2 \cap V_\partial(\mathbb{I}), \quad (4.4)$$

$$P^{n+1} \in V_1^N(\mathbb{I}), \quad g^{n+1} \in V_2^N(\mathbb{I}), \quad H^{n+1} \in V_2^N(\mathbb{I}) \cap H_g^1(\mathbb{I}). \quad (4.5)$$

such that

$$-\langle \boldsymbol{\varphi}, \mathcal{S}^{h,n}[\xi^{n+1}] \rangle_{C^n}^{h,*} + \langle \boldsymbol{\varphi}, \mathbf{U}^{n+1} \rangle_{C^n}^h = 0, \quad \forall \boldsymbol{\varphi} \in [V_2^N(\mathbb{I})]^2, \quad (4.6a)$$

$$\begin{aligned} & \langle \boldsymbol{\psi}, \xi^{n+1} \rangle_{C^n}^h + 2\mu_\Gamma \langle \mathbf{X}_s^n \cdot \boldsymbol{\psi}_s, \mathbf{X}_s^n \cdot \mathbf{U}_s^{n+1} \rangle_{C^n}^h + 2\mu_\Gamma \left\langle \frac{\boldsymbol{\psi}^r}{X^{r,n}}, \frac{U^{r,n+1}}{X^{r,n}} \right\rangle_{C^n}^h - \left\langle \mathbf{X}_s^n \cdot \boldsymbol{\psi}_s + \frac{\boldsymbol{\psi}^r}{X^{r,n}}, P^{n+1} \right\rangle_{C^n}^h \\ & + \langle \boldsymbol{\psi}, g^{n+1} \mathbf{n}^n \rangle_{C^n}^h = - \left\langle \boldsymbol{\psi}, \left(\alpha (H^n - c_0)^2 + \alpha_G K^n + \gamma \kappa_g^n \right) \mathbf{v}^n \right\rangle_{\partial C^n}, \quad \forall \boldsymbol{\psi} \in [V_2^N(\mathbb{I})]^2 \cap V_\partial(\mathbb{I}), \end{aligned} \quad (4.6b)$$

$$-\left\langle \boldsymbol{Q}, \mathbf{X}_s^n \cdot \mathbf{U}_s^{n+1} + \frac{U^{r,n+1}}{X^{r,n}} \right\rangle_{C^n}^h = 0, \quad \forall \boldsymbol{Q} \in V_1^N(\mathbb{I}), \quad (4.6c)$$

$$\left\langle \boldsymbol{\omega}, \frac{1}{\tau} (\mathbf{X}^{n+1} - \mathbf{X}^n) - \mathbf{U}^{n+1} \right\rangle_{C^n}^h = 0, \quad \forall \boldsymbol{\omega} \in [V_2^N(\mathbb{I})]^2, \quad (4.6d)$$

$$2 \langle \zeta, \mathbf{H}^{n+1} \rangle_{C^n}^h + \langle \zeta_s, \mathbf{X}_s^{n+1} \rangle_{C^n}^h + \left\langle \frac{\zeta^r}{X^{r,n}}, \frac{X^{r,n+1}}{X^{r,n}} \right\rangle_{C^n}^h = \langle \zeta, \mathbf{v}^n \rangle_{\partial C^n}, \quad \forall \zeta \in [V_2^N(\mathbb{I})]^2 \cap V_\partial(\mathbb{I}), \quad (4.6e)$$

$$\langle \eta, \mathbf{H}^{n+1} - \mathbf{n}^n \cdot \mathbf{H}^{n+1} \rangle_{C^n}^h = 0, \quad \forall \eta \in V_2^N(\mathbb{I}) \cap H_0^1(\mathbb{I}), \quad (4.6f)$$

$$\begin{aligned} & \langle \chi, g^{n+1} \rangle_{C^n}^h + \alpha \langle \chi_s, H_s^{n+1} \rangle_{C^n}^h = 2\alpha \left\langle \chi, (H^n - c_0) \left((H^n)^2 + H^n c_0 - K^n \right) \right\rangle_{C^n}^h \\ & + \langle \chi, -\gamma \kappa_n^n \rangle_{\partial C^n}, \quad \forall \chi \in V_2^N(\mathbb{I}). \end{aligned} \quad (4.6g)$$

Here, the discrete inner-product $\langle \cdot, \cdot \rangle_C^h$ is an approximation to the inner product $\langle \cdot, \cdot \rangle_C$ by Gauss-Legendre quadrature, and $\langle \cdot, \cdot \rangle_C^{h,*}$ is based on a special quadrature designed for the single-layer integral. Note that $\langle \boldsymbol{\varphi}, \mathcal{S}^{h,n}[\xi^{n+1}] \rangle_{C^n}^{h,*}$ is designed to approximate the term $\langle \boldsymbol{\varphi}, \mathcal{S}[\xi] \rangle_C$, which is a double-integral. We numerically approximate the double-integral by numerical quadrature and the single-layer integral \mathcal{S} is approximated by a discrete single-layer integral $\mathcal{S}^{h,n}$.

Due to the presence of a high-order spatial derivative, any explicit scheme suffers from numerical stiffness, imposing a severe constraint on the time step. While fully implicit schemes are generally more stable and can sometimes be unconditionally stable, the nonlinear nature of the equation makes such schemes challenging, as they result in nonlinear algebraic systems that are difficult and time-consuming to solve. The current numerical scheme (4.6) uses a semi-implicit time discretization designed to balance stability and efficiency. In this scheme, only the geometry and

boundary conditions are treated explicitly, while terms with high-order spatial derivatives are treated implicitly, thus removing the severe time-step constraint and yielding a linear system.

In the numerical scheme summarized in (4.6), due to the semi-implicit treatment, there are geometric quantities that depend on solutions at the time level t^n . Since \mathbf{X}^n is defined as a piecewise polynomial, we can directly compute its derivative \mathbf{X}_s^n and the normal derivative \mathbf{n}^n , $\boldsymbol{\mu}^n$, κ_n^n , and κ_g^n . The mean curvature H^n can be directly obtained from the solution at the previous time step, except for the first step, for which we use the analytical value as the initial condition for H . Recalling the expression in (3.5), we compute K^n by

$$K^n = \frac{X_s^{z,n}}{X^{r,n}} \left(2H^n - \frac{X_s^{z,n}}{X^{r,n}} \right), \quad (4.7)$$

for which we only have to compute the first derivative of \mathbf{X}^n .

The resulting coefficient matrix is mostly sparse, except for the block corresponding to the single-layer integral, which remains dense. However, due to the axisymmetric reduction, the problem is effectively one-dimensional, keeping the size of the linear system small. This enables efficient solution using direct methods, such as SparseLU [60].

4.2. Singularity capturing mesh refinement

The solution to the open membrane problem typically exhibits singular behavior near the open edge, such as ξ diverging as $|\xi| \sim d^{-1/2}$, where d is the distance to the edge. Such singularities are challenging to handle using a uniform computational mesh, leading to highly inaccurate results. It is well-known that local mesh refinement is preferred for resolving singular behavior. Here, we present a direct method for introducing local mesh refinement by modifying the initial parametrization of the generating curve.

For the initial reparametrization of \mathbf{X}_0 , if the parameter α is chosen to be proportional to the arc-length parameter of the initial curve, then a uniform discretization in α results in almost uniform spacing of points along the curve. Moreover, by carefully selecting the reparametrization, a uniform mesh in α can produce locally refined points along the curve, which is particularly useful for capturing singular behavior in the solution.

Let $\mathbf{X}_0(s)$, $s \in (0, L)$ represent the initial curve, parameterized by the arc-length s . We construct the locally refined reparametrization function $\Phi(\alpha)$ to satisfy the following properties:

1. The function Φ maps the two endpoints 0 and 1 to 0 and L , respectively, i.e., $\Phi(0) = 0$, $\Phi(1) = L$;
2. The reparametrization is non-singular, i.e., $\Phi'(\alpha) > 0$ for $\alpha \in (0, 1)$;
3. The reparametrization Φ has a local refinement property near the open edge, i.e., $\Phi'(\alpha)$ is close to 0 for all α such that $\mathbf{X}_0(\Phi(\alpha)) \in \partial_0\mathcal{C}$.

When both $\mathbf{X}_0(0)$ and $\mathbf{X}_0(1)$ represent open-edge ends, we choose the following function:

$$\Phi(\alpha) = (1 - \varepsilon)\Psi(\alpha) + \varepsilon L\alpha, \quad (4.8)$$

where $\varepsilon > 0$ is a small constant, typically chosen as $\varepsilon = 10^{-3}$, and Ψ is given by

$$\Psi(\alpha) = \frac{L}{2} (1 - \cos(\pi\alpha)). \quad (4.9)$$

Similarly, if only $\mathbf{X}_0(1)$ corresponds to an open edge, one may choose

$$\Psi(\alpha) = L \cos\left(\frac{\pi}{2}(1 - \alpha)\right). \quad (4.10)$$

It can be verified that Φ satisfies the three properties. We note that the regularization parameter ε is not essential and is introduced primarily for numerical convenience. Since the boundary condition involves geometric quantities such as κ_n and κ_g , which are treated explicitly, setting $\varepsilon = 0$ can lead to numerical instability due to poor parametrization at the endpoints, where $\Psi'(\alpha) = 0$. However, these geometric quantities at the endpoints are inherently independent of the parametrization and can be computed using an alternative and regular local parametrization of the generating curve. In such cases, one can simply set $\varepsilon = 0$. Under this cosine reparametrization, the mesh points become clustered near the endpoints. In particular, when $\varepsilon = 0$, the mesh spacing is approximately $h = \mathcal{O}(N^{-2})$ near the endpoints and $h = \mathcal{O}(N^{-1})$ in regions away from the endpoints, where N is the total number of mesh points.

4.3. Numerical quadrature for the singular integral

Assembling the coefficient matrix for the numerical scheme requires evaluating the double integral

$$I_{ij} = \langle \boldsymbol{\phi}^i, \mathcal{S}[\boldsymbol{\phi}^j] \rangle_C = \int_{\mathbb{I}} \int_{\mathbb{I}} X^r(\alpha) X^r(\alpha') \boldsymbol{\phi}^i(\alpha) \cdot \mathcal{S}(\alpha, \alpha') \boldsymbol{\phi}^j(\alpha') |\partial_\alpha \mathbf{X}(\alpha)| |\partial_\alpha \mathbf{X}(\alpha')| d\alpha' d\alpha, \quad (4.11)$$

where $\boldsymbol{\phi}^i$ and $\boldsymbol{\phi}^j$ are polynomial basis functions. Since the integral kernel $\mathcal{S}(\alpha, \alpha')$ is a linear combination of $K(k)$ and $E(k)$, where the former has a logarithmic-type singularity,

$$K(k) \sim -\frac{1}{2} \ln(1-k) + \mathcal{O}(1), \quad \text{as } k \rightarrow 1^-, \quad (4.12)$$

which corresponds to the limit $|\alpha - \alpha'| \rightarrow 0$. Standard numerical quadrature methods for smooth functions, such as tensor-product Gauss quadrature, encounter difficulties in approximating such singular integrals. When quadrature points lie along the diagonal $\alpha = \alpha'$, where the kernel becomes singular, the integrand becomes infinite, rendering these quadrature rules inapplicable. Even if care is taken to avoid direct evaluation at $\alpha = \alpha'$, convergence remains slow due to the unbounded derivatives of the integrand, which hinder error control. Alpert's quadrature [61] is well-suited for handling logarithmic-type singular integrals. This method achieves high-order accuracy for integrals of the form $\int_0^1 a(x) \ln(x) + b(x) dx$ where $a(x)$ and $b(x)$ are smooth, and has demonstrated excellent performance for similar problems. To accurately compute the singular double integral in this problem, we will design a specialized numerical quadrature scheme inspired by Alpert's rule, tailored for the singular behavior of the kernel.

After performing the cell-by-cell assembly of the matrix, it suffices to consider the case where the basis functions $\boldsymbol{\phi}^i$ and $\boldsymbol{\phi}^j$ have compact support on intervals \mathbb{I}_k and \mathbb{I}_l with $\mathbb{I}_k = (\alpha_{k-1}, \alpha_k)$. Under this condition, the double integral simplifies to

$$\hat{I}_{ij} = \int_{\mathbb{I}_k} \int_{\mathbb{I}_l} X^r(\alpha) X^r(\alpha') \boldsymbol{\phi}^i(\alpha) \cdot \mathcal{S}(\alpha, \alpha') \boldsymbol{\phi}^j(\alpha') |\partial_\alpha \mathbf{X}(\alpha)| |\partial_\alpha \mathbf{X}(\alpha')| d\alpha' d\alpha. \quad (4.13)$$

Three scenarios must be considered: (a) $k = l$, (b) $|k - l| = 1$, and (c) $|k - l| > 1$. For case (c), the integrand is smooth, allowing standard Gauss quadrature to be applied without modification. For both case (a) and (b), the integral has different types of singularities and certain care must be taken for numerical integration.

For case (a), the logarithmic singularity arises along the diagonal of the integration domain, i.e., when $\alpha = \alpha'$. The singular behavior of the integral \hat{I}_{ij} is therefore the same as the following canonical form:

$$I[f] = \int_0^1 \int_0^1 \ln|x-y| f(x, y) dx dy, \quad (4.14)$$

where $f(x, y)$ is assumed to be smooth in $[0, 1] \times [0, 1]$. We rewrite this integral as the sum of two integrals over triangular regions

$$I[f] = \iint_{\Delta_1} \ln|x-y| f(x, y) dx dy + \iint_{\Delta_2} \ln|x-y| f(x, y) dx dy, \quad (4.15)$$

where Δ_1 and Δ_2 are two right triangles separated by the diagonal $x = y$,

$$\Delta_1 = \{(x, y) : 0 < x < 1, 0 < y < x\}, \quad \Delta_2 = \{(x, y) : 0 < x < 1, x < y < 1\}. \quad (4.16)$$

The singularity now appears at one of the edges of each triangle. Due to symmetry, we only consider the integral on Δ_1 since the other one can be treated similarly. By introducing the change of variables in Δ_1 ,

$$\begin{pmatrix} x \\ y \end{pmatrix} = \begin{pmatrix} \xi + \eta - \xi\eta \\ \eta - \xi\eta \end{pmatrix}, \quad \xi \in (0, 1), \eta \in (0, 1). \quad (4.17)$$

the integral can be reformulated as an integral over a unit square

$$\iint_{\Delta_1} \ln|x-y| f(x, y) dx dy = \int_0^1 \int_0^1 f(x(\xi, \eta), y(\xi, \eta)) (1-\xi) \ln \xi d\xi d\eta, \quad (4.18)$$

where the logarithmic singularity only appears in the ξ -direction as $\xi \rightarrow 0$, while the integrand in the η -direction remains regular for fixed ξ . After the transformation, the application of Alpert's quadrature rule becomes straightforward. By applying Alpert's rule in the ξ -direction and the Gauss quadrature in the η -direction, we obtain the following approximation,

$$\int_0^1 \int_0^1 f(x(\xi, \eta), y(\xi, \eta))(1 - \xi) \ln \xi \, d\xi \, d\eta \approx \sum_{i=1}^{N_1} \sum_{j=1}^{N_2} w_{1,i} w_{2,j} f(x(\xi_i, \eta_j), y(\xi_i, \eta_j))(1 - \xi_i) \ln \xi_i, \quad (4.19)$$

where $\{(\xi_i, w_{1,i})\}_{i=1}^{N_1}$ and $\{(\eta_j, w_{2,j})\}_{j=1}^{N_2}$ are the quadrature points and weights for Alpert's rule and Gauss-Legendre quadrature on $(0, 1)$, respectively.

For case (b), the singularity occurs at the corner of the rectangle $\mathbb{I}_k \times \mathbb{I}_l$. We consider the integral as follows

$$I = \int_0^1 \int_{-1}^0 \ln |x - y| f(x, y) \, dx \, dy = - \int_0^1 \int_0^1 \ln(x + y) f(-x, y) \, dx \, dy. \quad (4.20)$$

The logarithmic-type singularity is located at the corner $(0, 0)$ of the rectangular integration domain. Let us split the I into integrals over two triangular regions

$$I = - \iint_{\Delta_1} \ln(x + y) f(-x, y) \, dx \, dy - \iint_{\Delta_2} \ln(x + y) f(-x, y) \, dx \, dy, \quad (4.21)$$

where Δ_1 and Δ_2 are two right triangles separated by the anti-diagonal $y = 1 - x$,

$$\Delta_1 = \{(x, y) : 0 < x < 1, 0 < y < 1 - x\}, \quad \Delta_2 = \{(x, y) : 0 < x < 1, 1 - x < y < 1\}. \quad (4.22)$$

Then, the integral over Δ_1 is singular, while the integral over Δ_2 is regular. By introducing the change of variable as follows,

$$\begin{pmatrix} x \\ y \end{pmatrix} = \begin{pmatrix} \xi - \xi\eta \\ \xi\eta \end{pmatrix}, \quad \xi \in (0, 1), \eta \in (0, 1). \quad (4.23)$$

The singular integral over Δ_1 can be reformulated as an integral over a unit square

$$\iint_{\Delta_1} \ln(x + y) f(-x, y) \, dx \, dy = \int_0^1 \int_0^1 f(-x(\xi, \eta), y(\xi, \eta)) \xi \ln \xi \, d\xi \, d\eta, \quad (4.24)$$

where the logarithmic singularity is only in the ξ -direction. By applying Alpert's rule in the ξ -direction and the Gauss quadrature rule in the η -direction, we obtain the following approximation,

$$\int_0^1 \int_0^1 f(-x(\xi, \eta), y(\xi, \eta)) \xi \ln \xi \, d\xi \, d\eta \approx \sum_{i=1}^{N_1} \sum_{j=1}^{N_2} w_{1,i} w_{2,j} f(-x(\xi_i, \eta_j), y(\xi_i, \eta_j)) \xi_i \ln \xi_i. \quad (4.25)$$

Similarly, we can introduce a change of variable to reformulate the integral over Δ_2 as a regular integral over a unit square and apply the tensor product Gauss quadrature rule for the numerical integration.

5. Numerical experiments

In this section, we present numerical experiments to validate our numerical method for simulating an open membrane interacting with a surrounding fluid flow. To ensure generality and facilitate comparison with related studies, we introduce the nondimensional form of the governing equations. Let L and T represent the characteristic length and time scales, respectively. We define the following nondimensional variables

$$\begin{aligned} \tilde{\mathbf{x}} &= \frac{\mathbf{x}}{L}, \quad \tilde{t} = \frac{t}{T}, \quad \tilde{\mathbf{u}} = \frac{T\mathbf{u}}{L}, \quad \tilde{\mathbf{U}} = \frac{T\mathbf{U}}{L}, \quad \tilde{p} = \frac{Tp}{\mu}, \quad \tilde{P} = \frac{TP}{\mu_\Gamma}, \\ \tilde{H} &= LH, \quad \tilde{K} = L^2K, \quad \tilde{\boldsymbol{\sigma}} = \frac{T}{\mu}\boldsymbol{\sigma}, \quad \tilde{\boldsymbol{\sigma}}_\Gamma = \frac{T}{\mu_\Gamma}\boldsymbol{\sigma}_\Gamma. \end{aligned} \quad (5.1)$$

where the tildes denote nondimensional quantities. The nondimensional stress tensors can then be expressed as

$$\begin{aligned}\tilde{\boldsymbol{\sigma}} &= -\tilde{p}\mathbf{I} + \tilde{\nabla}\tilde{\mathbf{u}} + \tilde{\nabla}\tilde{\mathbf{u}}^\top, \\ \tilde{\boldsymbol{\sigma}}_\Gamma &= -\tilde{P}\tilde{\mathbf{P}}_\Gamma + \tilde{\mathbf{P}}_\Gamma \left(\tilde{\nabla}_\Gamma\tilde{\mathbf{U}} + \tilde{\nabla}_\Gamma\tilde{\mathbf{U}}^\top \right) \tilde{\mathbf{P}}_\Gamma.\end{aligned}\quad (5.2)$$

Substituting these nondimensional variables into the governing equations (2.24) and omitting the tildes for clarity, the nondimensional equations are given by

$$-\nabla \cdot \boldsymbol{\sigma} = \mathbf{0}, \quad \text{in } \Omega, \quad (5.3a)$$

$$-\nabla \cdot \mathbf{u} = 0, \quad \text{in } \Omega, \quad (5.3b)$$

$$[[\boldsymbol{\sigma}\mathbf{n}]] - \beta\nabla_\Gamma \cdot \boldsymbol{\sigma}_\Gamma + (\Delta_\Gamma H + 2(H - H_0)(H^2 + H_0H - K))\mathbf{n} = \mathbf{0}, \quad \text{on } \Gamma, \quad (5.3c)$$

$$-\nabla_\Gamma \cdot \mathbf{U} = \mathbf{0}, \quad \text{on } \Gamma, \quad (5.3d)$$

$$\mathbf{u} = \mathbf{U}, \quad \text{on } \Gamma, \quad (5.3e)$$

$$\partial_t \mathbf{X} = \mathbf{U}, \quad \text{on } \Gamma, \quad (5.3f)$$

$$\beta\boldsymbol{\sigma}_\Gamma \mathbf{v} + \left((H - H_0)^2 + \gamma_g K + \gamma_l \kappa_g \right) \mathbf{v} = \mathbf{0}, \quad \text{on } \partial\Gamma, \quad (5.3g)$$

$$\nabla_\Gamma H \cdot \mathbf{v} - \gamma_g \tau'_g + \gamma_l \kappa_n = 0, \quad \text{on } \partial\Gamma, \quad (5.3h)$$

$$H - H_0 + \gamma_g \kappa_n = 0, \quad \text{on } \partial\Gamma, \quad (5.3i)$$

where the time scale is set as $T = L^3\mu/\alpha$, and we have the following nondimensional parameters

$$\beta = \frac{\mu_\Gamma}{L\mu}, \quad \gamma_g = \frac{\alpha_G}{\alpha}, \quad \gamma_l = \frac{\gamma L}{\alpha}, \quad H_0 = Lc_0. \quad (5.4)$$

5.1. Annular-shaped planar membrane

We consider the case where the membrane is planar and has an annular shape,

$$\Gamma = \left\{ (x, y, z) : z = 0, r = \sqrt{x^2 + y^2} \in (R_i, R_o) \right\}, \quad R_o > R_i > 0, \quad (5.5)$$

where R_i, R_o are the inner and outer radii of the membrane, respectively. For such a configuration, our PDE model in Equations (2.24) reduces to a set of equations that are similar to the one in [58]. Particularly, when the outer radius of the annular goes to infinite, closed form solutions for the velocity field and the membrane tension can be constructed analytically, allowing us to validate our numerical method by comparing with the analytical solution. In this case, the bending energy of the membrane is ignored and the dynamics of the membrane is only driven by the line tension on the open edges. Therefore, bending rigidities and the spontaneous curvature are assumed to be zero.

First, we perform the convergence check for the velocity field on the planar membrane. The planar membrane only has nonzero radial velocity and, due to the inextensible condition, the radial velocity is given by

$$U^r(r) = \frac{F}{r}, \quad (5.6)$$

where F is an integration constant that can be explicitly computed when the outer radius of the membrane is infinite. For a finite membrane, the constant F can be computed as follows: We numerically solve the full PDE model for one time step to obtain the velocity field and compute the error of the radial velocity, only up to a multiplicative constant, to assess the accuracy of the numerical method. The parameters used are chosen as $\beta = \gamma_l = 1$, and the membrane is defined with initial radii $R_{i,0} = 1$ and $R_{o,0} = 2$. After obtaining the numerical solution U_h^r , on noting that $F \equiv rU^r(r)$, we estimate the constant F by the formula

$$F_h = \frac{\int_\Gamma rU_h^r d\mu_\Gamma}{|\Gamma|} = \frac{\int_{R_i}^{R_o} r^2 U_h^r(r) dr}{\int_{R_i}^{R_o} r dr}. \quad (5.7)$$

Next, the error is defined as:

$$\|e_{U,h}\|_{L^2(\Gamma)} = \left(\int_{R_i}^{R_o} r \left(U_h^r(r) - \frac{F_h}{r} \right)^2 dr \right)^{\frac{1}{2}}, \quad (5.8)$$

where all the integrals are evaluated using composite Gaussian quadrature. To demonstrate the advantage of the singularity capturing mesh refinement strategy, we compare the numerical errors obtained by using a uniform mesh and a locally refined mesh with different mesh size $N = 4, 8, \dots, 128$. The results shown in the left panel of Figure 2 demonstrates that the locally refined mesh generates higher convergence rate than the uniform mesh for the radial velocity. To demonstrate the effectiveness of the local mesh refinement, we vary the parameter ϵ to check the ability of the numerical scheme to capture the singularity of the single-layer density ξ . In the planar configuration, ξ only has non-zero radial component ξ^r . We use the same mesh size $N = 32$ and plot the absolute value ξ^r in the right panel of Figure 2. When the mesh is uniform, corresponding to $\epsilon = 1$, the result generates noticeable oscillation in

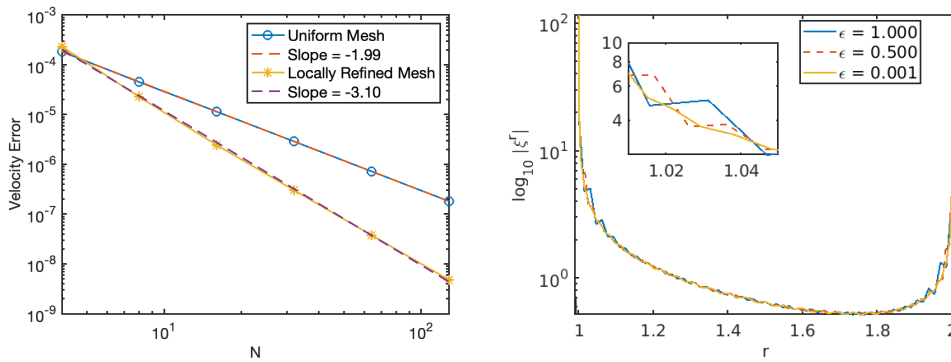


Figure 2: Left: numerical error of the radial velocity for different mesh size using both uniform mesh and locally refined mesh; Right: radial single-layer density ξ^r computed using differential regularizing parameters $\epsilon = 1, 0.5, 0.001$ with $N = 32$.

the vicinity of the open edge where ξ^r is expected to diverge. On the contrary, When local mesh refinement is applied, corresponding to $\epsilon = 0.001$, oscillation near the open edge is suppressed and the predicted value at $x = 1$ is much larger compared with uniform mesh, suggesting the local mesh refinement strategy increases the capability of capturing the singularity behavior of the solution near the open edge.

As the outer radius R_o goes to infinity, an explicit expression for the value of the constant F is available. Since we can only apply a finite number of R_o in the numerical method, we fix the initial inner radius as $R_{i,0} = 1$ and successively increase the initial outer radius $R_{o,0}$ to approximate the case where $R_o = \infty$, and compare the numerical result of $F(t)$ with the analytical result. We set the computation mesh as $N = 32$ with local mesh refinement for $\epsilon = 0.001$ and time step as $\Delta t = 0.01$ for the computation. The result is shown in Figure 3. The time is rescaled to $t/\tau_{2,0}$ where $\tau_{2,0} = \mu R_{i,0}^2/\gamma$ is the same as the one defined in [58]. It can be observed that as the value $R_{o,0} - R_{i,0}$ increase, the estimated value of F is closer to the limiting case where $R_{o,0} - R_{i,0}$, demonstrating the convergence of the numerical solution. We also use the current numerical method to compute the closing dynamics of the membrane hole for different parameter μ_Γ/μ , and compare the computed value of F and hole area with the exact solutions computed using the technique presented in [58]. The analytical and numerical solution for F against t are shown in Figure 4. Those for the hole area A against t are shown in Figure 5.

5.2. Equilibrium Shapes

Here we compute the equilibrium shapes of an open membrane and compare the results with those reported in [1] and [39]. We simulate the relaxation of an inextensible elastic open membrane to equilibrium where the fluid flow ceases ($\mathbf{u} = 0$ and $\mathbf{U} = 0$) and the membrane shape Γ is independent of time. Under the assumption of membrane inextensibility, the membrane area remains constant during the relaxation process, and is solely determined by its initial configuration. Consequently, the equilibrium shape depends on the initial shape and the following key parameters: $\gamma_g = \alpha_G/\alpha$, $\tilde{\gamma} = \gamma/\alpha$, and c_0 .

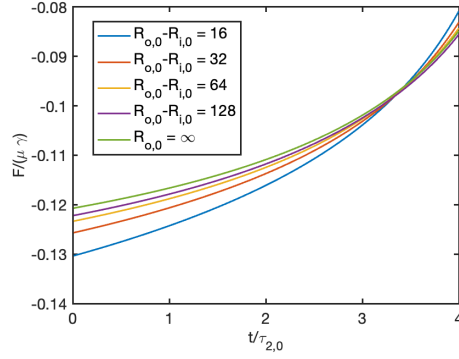


Figure 3: Numerical solution of F with difference membrane width $R_{o,0} - R_{i,0} = 16, 32, 64, 128$ compared with analytical solution of F for $R_{o,0} = \infty$.

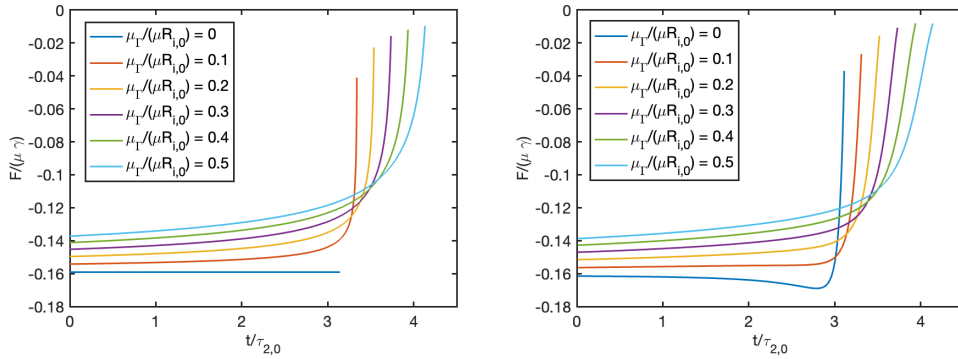


Figure 4: Exact solution (left) and numerical solution (right) for the constant F over time for different viscosity ratio $\mu_{\Gamma}/(\mu R_{i,0}) = 0, 0.1, \dots, 0.5$.

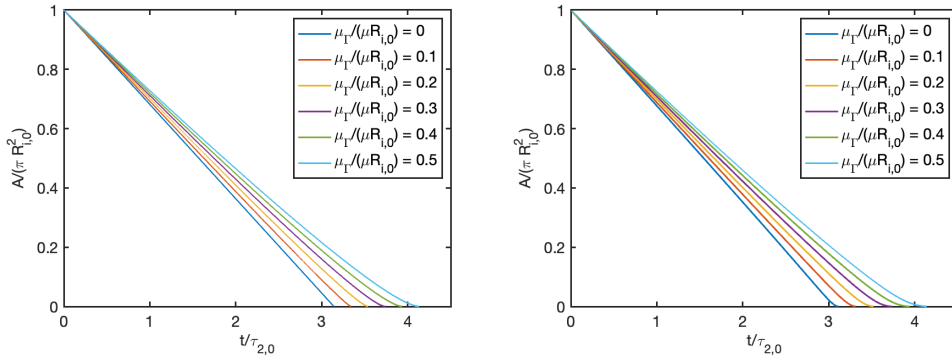


Figure 5: Exact solution (left) and numerical solution (right) for the evolution of the hole area A over time for different viscosity ratio $\mu_{\Gamma}/(\mu R_{i,0}) = 0, 0.1, \dots, 0.5$.

It is worth noting that our inextensibility assumption for the membrane differs from the extensible membrane model in [39], where a surface energy term associated with surface tension is included. In their formulation, surface tension is prescribed as a constant parameter, whereas in our approach, it emerges naturally as a Lagrange multiplier to enforce inextensibility. However, at equilibrium, both models have a constant surface tension across the membrane, enabling meaningful comparisons of equilibrium shapes.

Table 1

Parameter values for each case.

Case	γ_g	$c_0 (\mu m^{-1})$	$\tilde{\gamma} (\mu m^{-1})$	$A_0 (\mu m^2)$
1	-0.122	0.2	0.65	27.61
2	-0.122	0.2	0.78	23.15
3	-0.122	0.2	0.79	18.42

We examine three cases for numerical comparison, where the spontaneous curvature and reduced Gaussian curvature rigidity are fixed as $\gamma_g = -0.122$ and $c_0 = 0.2 \mu m^{-1}$. The negative value of γ_g indicates that surfaces with positive Gaussian curvature are energetically more favorable than those with negative Gaussian curvature. The initial membrane shapes are selected to ensure their areas match the equilibrium areas reported in [39]. The parameter values for each case are summarized in Table 1. The initial membrane shapes are selected to be close to the expected equilibrium configurations, as the membrane energy landscape can exhibit multiple equilibrium states. The dynamical equations are then solved over time until the total membrane energy ceases to decrease significantly. The computation is terminated when the relative change in total energy falls below 10^{-6} . The time evolution of the total energy \mathcal{E} for the three cases is shown in Figure 6. The corresponding equilibrium shapes are presented in Figure 7.

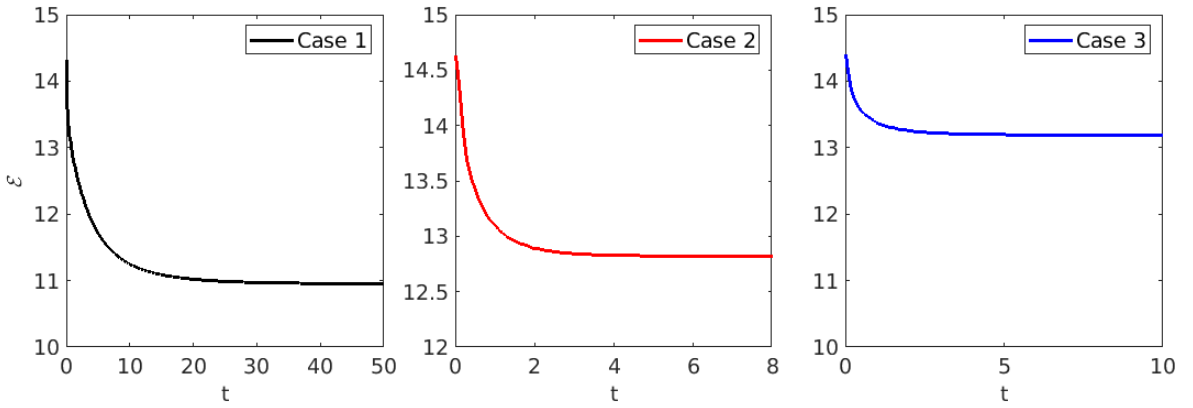
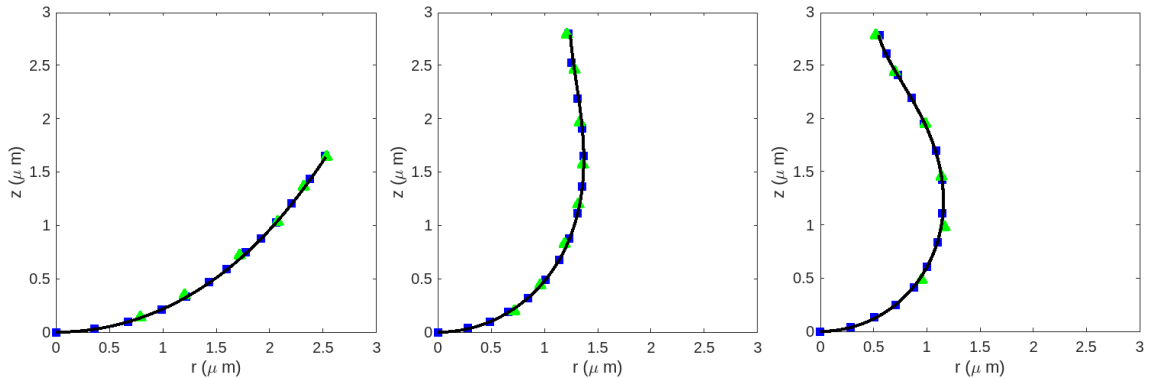

Figure 6: Time evolution of the total energy of the membrane for the three cases.


Figure 7: Equilibrium shapes of an open membrane: the black solid curves are the numerical solutions obtained using our method; the blue squares depict the numerical results from [39]; the green triangles show the experimental data from Fig. 3 (I to K) in [1]. From left to right are cases 1, 2 and 3 with reduced line tension $\tilde{\gamma} = 0.65, 0.78, 0.79 (\mu m^{-1})$, and initial areas of $27.61, 23.15, 18.42 (\mu m^2)$ respectively.

5.3. Membrane dynamics from a spherical cap

In this example, we investigate the dynamic behavior of an open membrane starting from an initial spherical cap shape. Previous numerical studies of membranes with a pore often assume that the membrane retains a spherical cap geometry throughout its evolution. This assumption simplifies the problem to a set of ODEs that govern a few geometric parameters [5, 46]. The justification for this approximation lies in the fact that a closed spherical membrane with constant mean curvature satisfies the equilibrium condition for normal stress balance. However, this assumption becomes less realistic in scenarios where the membrane has an open pore, particularly near the free edge [62].

Using our numerical method, we simulate the dynamics of an open membrane initialized as a spherical cap. The parameters are set as $\beta = 1$ and $\gamma_g = \gamma_l = H_0 = 0$, corresponding to the Willmore energy and zero line tension. The initial shape is defined by the generating curve:

$$X_0^r(s) = \sin(s), \quad X_0^z(s) = -\cos(s), \quad s \in [0, 0.9\pi]. \quad (5.9)$$

The numerical results are shown in Figure 8 and Figure 9. Initially, the membrane maintains a spherical cap shape. Over time, bending forces drive both bulk fluid flow and surface flow, causing the membrane to flatten. As the membrane evolves, deviations from the spherical cap geometry emerge, particularly near the open edge, where a neck-like structure begins to form.

This deviation can be understood through the geometric boundary condition $H = 0$, as specified in (5.3i). While a spherical cap inherently possesses a non-zero constant mean curvature, this boundary condition is incompatible with the spherical cap assumption, leading to geometric deviations near the free edge.

Next, we incorporate the influence of line tension by setting $\gamma_l = 0.5$. The line tension introduces an additional force along the open edge, acting to minimize its length and counteracting the bending force. The computation is terminated when the pore becomes sufficiently small to avoid numerical instabilities. As shown in Figure 10, a neck forms at an early stage due to the boundary condition on the mean curvature. Eventually, the pore closes while preserving the neck structure. In contrast, regions of the membrane far from the open edge maintain a nearly spherical cap shape.

These findings indicate that while the spherical cap assumption can provide an approximate description of the global membrane shape, particularly during early stages of pore formation, it fails to capture the detailed local behavior near the open edge. The imposed geometric boundary conditions play a crucial role in determining these local deviations.

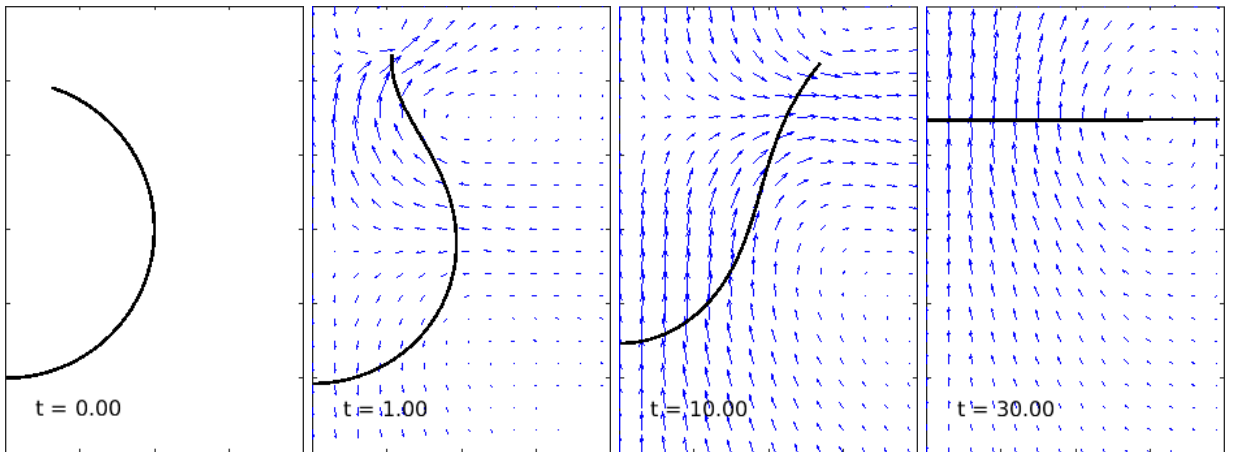


Figure 8: Section view of the generating curve of the membrane and the velocity field of the fluid flow for $t = 0, 1, 10, 30$.

We also plot the time evolution of the membrane area for the above two initial configurations in Figure 11. Since the membrane is locally inextensible, its total area should remain constant over time. Although the numerical solution introduces a slight variation due to discretization errors, the relative change in area remains below 0.05% in both cases, demonstrating that the numerical method effectively preserves the area.

As reported in [62], for small but non-zero $\epsilon = \gamma_l^{-1}$, an equilibrium membrane shape introduces an elastic boundary layer near the open edge. In our dynamic evolution equation, a similar boundary layer structure emerges during the membrane's evolution. To investigate this boundary layer more closely, we systematically reduce γ_l^{-1} from 1 to 0.01.

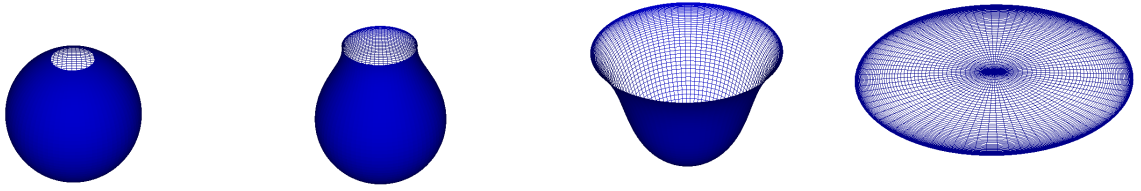


Figure 9: Three-dimensional view of the membrane shape for $t = 0, 1, 10, 30$.

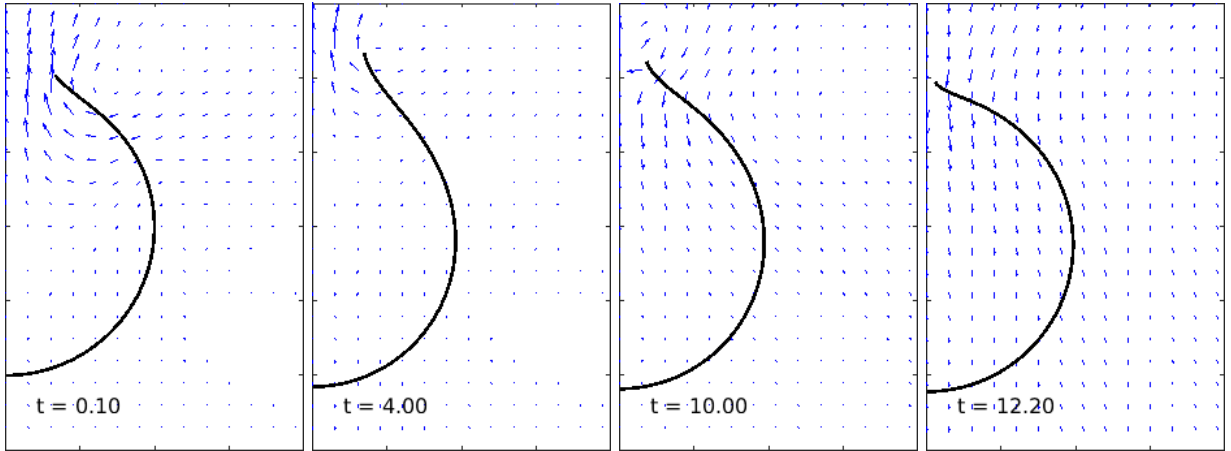


Figure 10: Section view of the generating curve of the membrane and the velocity field of the fluid flow for $t = 0.1, 4, 10, 12.2$.

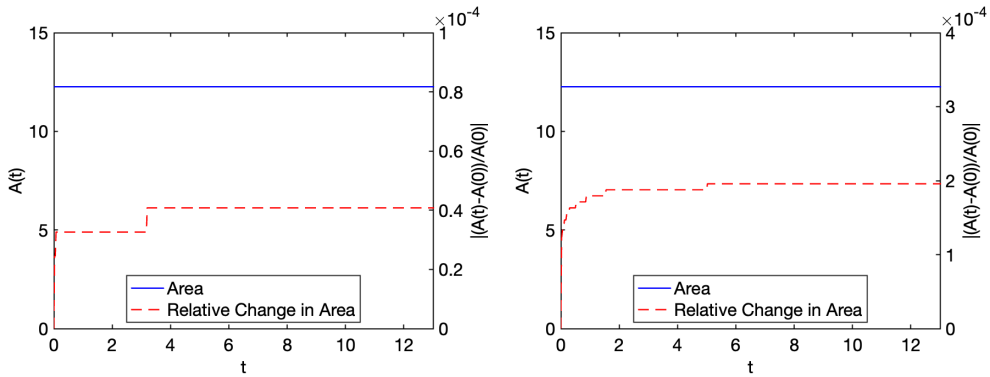


Figure 11: Time evolution of the membrane area and the corresponding relative change. Left: area profile for the flattening membrane; Right: area profile for the closing membrane.

Figure 12 illustrates the mean curvature profiles for three different values of the ratio $\gamma_l^{-1} = 1, 0.1, 0.01$ and shows the variation of mean curvature along the arc-length parameter of the generating curve. The endpoint $s = 0$ corresponds to the closed end in contact with the z -axis, while the other endpoint represents the open edge. The results reveal that as γ_l^{-1} decreases, the boundary layer near the open edge becomes increasingly sharp and localized. For larger γ_l^{-1} , the mean curvature varies smoothly across the membrane, and the boundary layer effect is less pronounced. As γ_l^{-1} becomes smaller, the curvature gradient steepens near the open edge, indicating a stronger influence of the elastic boundary layer. This behavior suggests that the parameters γ_l^{-1} play a critical role in controlling the membrane's

local geometry near the open boundary. When γ_l^{-1} is large, bending stiffness dominates, leading to a more uniform membrane profile. In contrast, when γ_l^{-1} is small, the interplay between line tension and bending forces results in a highly localized boundary layer near the open edge. These findings highlight the importance of accurately resolving the boundary layer structure in numerical simulations. Failure to capture this sharp transition can lead to significant inaccuracies in predicting the membrane's behavior near the open edge, particularly in scenarios where local geometric effects are dominant.

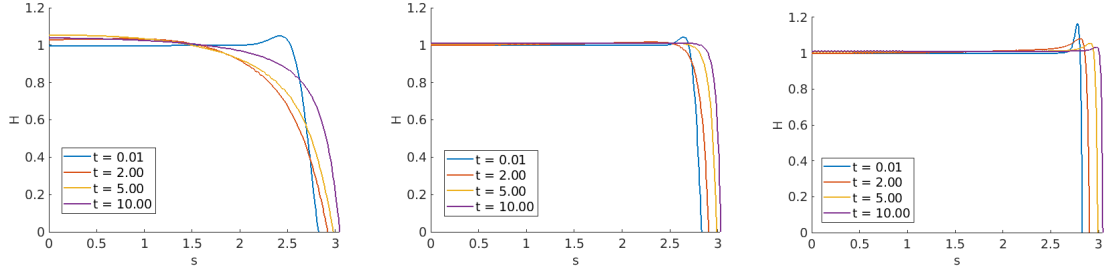


Figure 12: Numerical solution of the mean curvature on the membrane at different time vs. arc-length parameter for $\gamma_l^{-1} = 1, 0.1, 0.01$ from left to right. The endpoint $s = 0$ is the closed end in contacting with the z -axis, the other endpoint is the open edge.

We compare our PDE model (2.24), which allows the membrane to adopt arbitrary shapes, with a simplified ODE model based on the spherical cap assumption. The ODE model assumes that the membrane maintains a spherical cap geometry throughout its evolution. This configuration is parameterized by three key variables: the sphere radius R , the cap angle α , and the center position z_0 . Using an energy variational approach and incorporating viscous force calculations from [46], we derive an ODE system governing the dynamics of R , α , and z_0 . The detailed derivation is provided in Appendix C. Unlike the extensible membrane model in [46], where surface tension is prescribed as a constant parameter, our model enforces local inextensibility. In this framework, surface tension emerges as a Lagrange multiplier, ensuring that the membrane area remains constant throughout its evolution.

For numerical simulations, we adopt physical parameters from [46]: an initial sphere radius of $20 \mu\text{m}$, an initial hole radius of $6 \mu\text{m}$, a line tension of 12 pN , fluid viscosity of $1 \text{ mPa}\cdot\text{s}$, and membrane viscosity of $3 \times 10^{-9} \text{ Pa}\cdot\text{m}\cdot\text{s}$. The characteristic spatial and time scales are chosen as $L = 20 \mu\text{m}$ and $T = 1 \text{ s}$. Both the PDE and ODE models are initialized with the same shape described by (5.9). The numerical solutions from both models are presented in Figure 13. For such a parameter, the boundary layer is thin and shape of the membrane predict by the PDE and ODE matches well in regions away from the open edge.

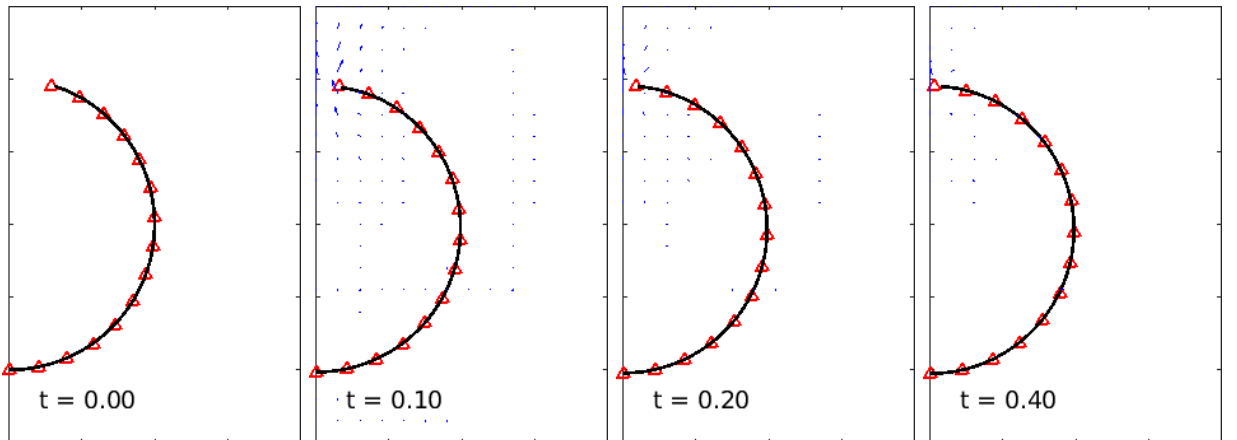


Figure 13: Numerical solutions for the open membrane obtained by solving the PDE model (solid dark line) and simplified ODE model (red triangles).

Figure 14 shows the evolution of the hole radius predicted by both the ODE and PDE models, with varying mesh refinement levels. At early stages ($t < 0.2$), the PDE model converges as the mesh is refined, and the ODE predictions closely match the PDE results. However, as the hole shrinks, discrepancies between the models become apparent. The ODE model predicts an exponential decay of the hole radius to zero, while the PDE model indicates that the hole radius approaches a steady state before further closure. In Figure 15, we compare the averaged surface tension

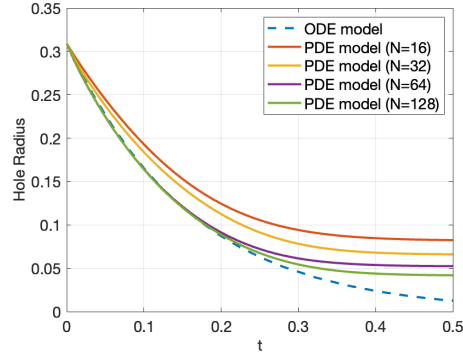


Figure 14: Hole radius of the spherical cap-shaped membrane predicted by the PDE and ODE models.

predicted by the ODE model with the effective surface tension obtained from the PDE model. In the PDE simulation, the surface tension evolves toward a limiting value of approximately -400 and becomes nearly uniform across the membrane, indicating equilibrium. In contrast, the ODE model predicts a continuous decrease in surface tension, even when the hole becomes extremely small, with values significantly larger than those observed in the PDE model. This inconsistency highlights the inadequacy of the spherical cap assumption, particularly when considering the localized behavior of the membrane near the open edge.

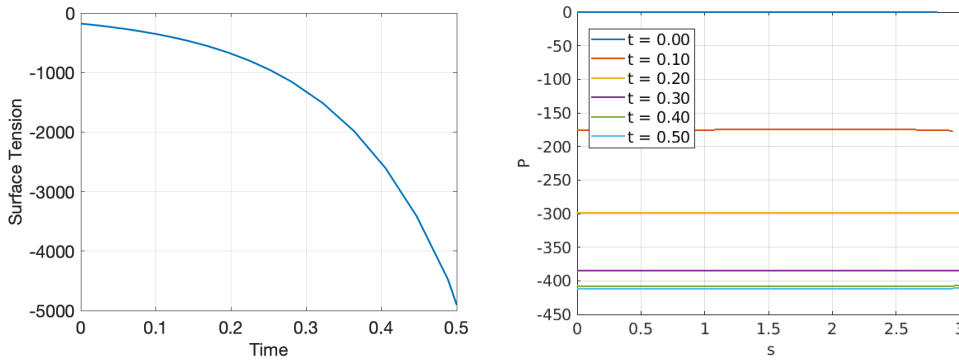


Figure 15: Left: Surface tension predicted by the ODE model over time. Right: Surface tension predicted by the PDE model, where the x -axis represents the generating curve parameter (with $\alpha = 1$ denoting the membrane edge).

These differences highlight the impact of the assumptions underlying each model. The spherical cap assumption simplifies the analysis but fails to capture the intricate local behavior near the membrane edge. In contrast, the PDE model provides a more detailed and accurate description of membrane dynamics, especially when boundary effects and local geometric constraints dominate.

It is worth emphasizing that the assumption of membrane extensibility in Rolf's model [46] leads to notable differences in the observed phenomena, such as the exponential growth of the hole radius in the early stages. Lipid bilayer membranes are known to resist changes in surface area, typically allowing only around 10% variation. For an initially stretched, extensible membrane, even minimal extensibility can drive rapid pore expansion due to surface tension effects. In such scenarios where surface area variation plays a significant role, a nearly inextensible membrane

model might be able to capture these realistic phenomenon, as opposed to assuming perfect inextensibility. We aim to explore such refinements in future work.

5.4. Membrane with different initial shapes

In this example, we investigate the dynamics of lipid membranes starting from various initial shapes beyond the spherical cap configuration. We begin by examining a membrane initialized as a flat sheet to simulate the evolution of a closed vesicle originating from an open planar membrane. A flat sheet with zero spontaneous curvature represents a steady-state configuration under significant bending force and line tension. However, introducing a small degree of spontaneous curvature induces membrane bending, thereby amplifying the role of line tension in determining the membrane shape. For this study, the dimensionless parameters are set as $\gamma_g = 0$, $\beta = 1$, and $H_0 = 0.1$.

First, we consider a small line tension value of $\gamma_l = 1$. Numerical results, shown in Figure 16, indicate that the small spontaneous curvature causes the membrane to bend slightly, approaching a near-equilibrium configuration. However, the low line tension is insufficient to drive the membrane toward full closure into a vesicle.

Subsequently, we increase the line tension to $\gamma_l = 5$. As illustrated in Figure 17, the elevated line tension actively drives the open edge of the membrane to close, forming a nearly closed vesicle structure.

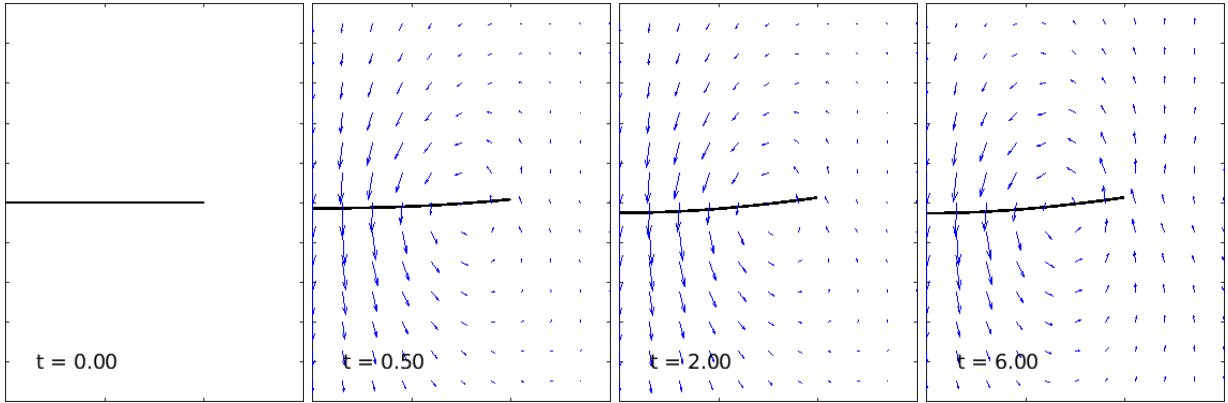


Figure 16: Numerical solutions for an open membrane starting from a flat sheet with a weak line tension of $\gamma_l = 1$ at time points $t = 0, 0.5, 2, 6$.

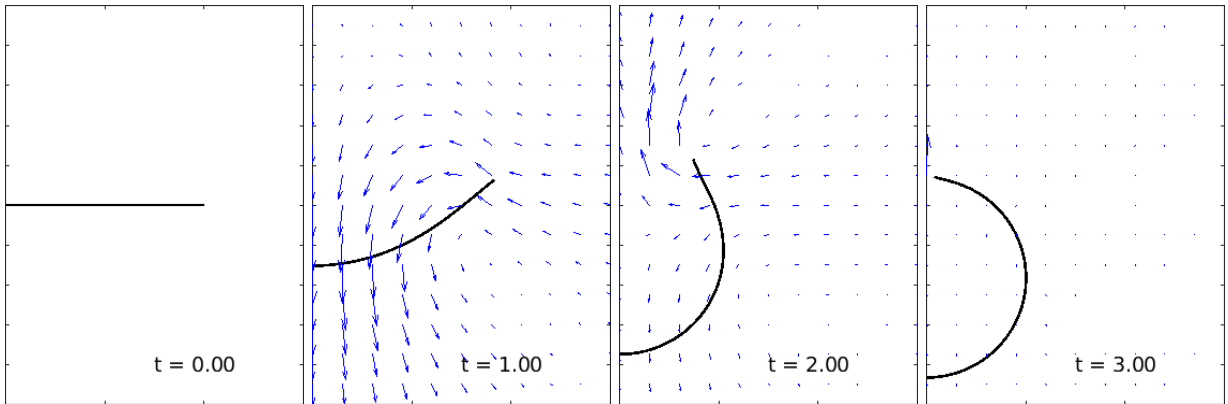


Figure 17: Numerical solutions for an open membrane starting from a flat sheet with a strong line tension of $\gamma_l = 5$ at time points $t = 0, 1, 2, 3$.

To further investigate membrane dynamics, we consider an initial membrane shape resembling a biconcave red blood cell with a small pore. The parametric form of this shape is given by

$$\begin{aligned} r(\eta) &= 2\sqrt{\eta(1-\eta)}, & z(\eta) &= 0.7(2\eta-1) - 0.6(2\eta-1)^3 + 0.05(2\eta-1)^5, \\ \eta(s) &= 0.475(1 - \cos(\pi s)), & s &\in [0, 1]. \end{aligned} \quad (5.10)$$

Using the same dimensionless parameters as before ($\gamma_g = 0$, $\beta = 1$, and $H_0 = 0.1$), we first consider a strong line tension ($\gamma_l = 5$). As shown in Figure 18, the strong line tension drives the small pore to close rapidly, leaving the enclosed volume of the cell essentially unchanged, meaning the resulting steady state is not affect much. This scenario suggests efficient healing of membrane damage without significant deformation.

Conversely, when the line tension is reduced to $\gamma_l = 1$, the pore does not close immediately. Instead, the membrane begins to deform into an alternative configuration, preventing it from returning to a closed vesicle state. This behavior, illustrated in Figure 19, underscores the critical role of line tension in the formation, stability, and repair processes of lipid membranes.

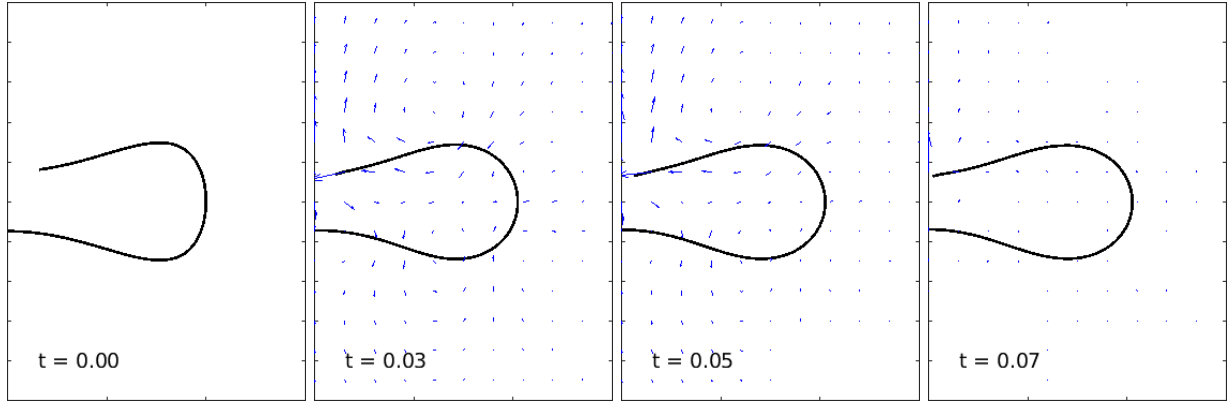


Figure 18: Numerical solutions for an open membrane starting from a biconcave red blood cell with a small pore for $\gamma_l = 5$.

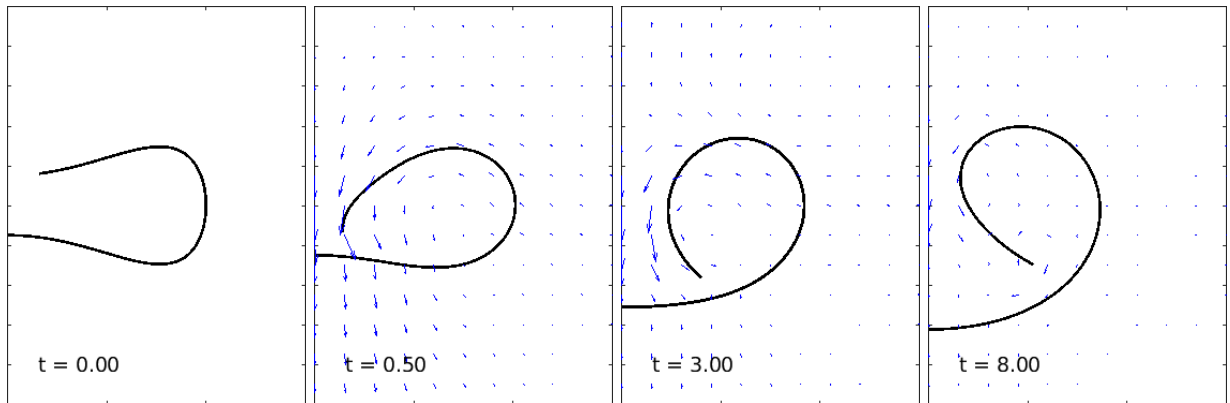


Figure 19: Numerical solutions for an open membrane starting from a biconcave red blood cell with a small pore for $\gamma_l = 1$.

6. Discussion

For an open, inextensible membrane immersed in Stokes flow, we derive a continuum model based on the principle of maximum dissipation within an energy variational framework. The membrane is represented as a zero-thickness open surface endowed with a membrane energy comprising the Helfrich bending energy and a line tension along its open edge. Dissipative effects from both the bulk and membrane viscosities are incorporated via Rayleigh dissipation functionals, while incompressibility of the surrounding fluid and inextensibility of the membrane are enforced through Lagrange multipliers. Taking first variations and balancing surface and boundary forces yields the coupled PDEs governing membrane–fluid interactions.

To conduct numerical simulations for the PDE model, we consider the axisymmetric case for both the membrane and fluid flow. For this scenario, we adopt a boundary integral formulation, reducing the 3D problem into a 1D problem

along the generating curve. Due to the complex coupling between the boundary integral and geometric quantities, we developed a finite-element-based numerical scheme by rewriting the high-order PDE into a weak mixed form, which only contains first derivatives. The time discretization is semi-implicit: low-order derivatives, nonlinear terms and boundary terms are treated explicitly, while high-order derivatives, linear terms are treated implicitly. This ensures that the final scheme is both stable and can be solved efficiently. The single-layer density typically exhibits singular behavior near the open edge. To address this, we designed a local mesh refinement strategy that increases the resolution of the computational mesh near the open edge, improving the scheme's ability to capture singularities. Using the developed axisymmetric numerical scheme, we applied it to model open membranes in different cases. The present numerical method can be applied to investigate the behavior of open membranes interacting with the bulk flow, such as the relaxation dynamics of membranes under the influence of the bulk fluid and the dynamics of pores in membranes influenced by fluid leakage.

Lipid bilayer membranes are nearly inextensible, and a weak area compressibility may result in fluid leakage that alters both the membrane dynamics [63] and the pore dynamics [46]. How does such weak area compressibility affect the transition from a (closed) vesicle to an open membrane? To answer this question we have been working on improving our PDE model for the lipid bilayer membrane to account for the physical area compressibility within the boundary integral framework.

Furthermore the current numerical method can be improved in several directions. By carefully studying the singularity behavior of the solution near the open edge, it should be possible to develop a high-order numerical method that incorporates an analytical expression for the singularity structure, reducing the need for mesh refinement. Developing numerical schemes to perform full 3D simulations for membranes with general shapes is another challenging but interesting direction.

Appendix

A. Derivation of the axisymmetric single-layer integral

Suppose the axisymmetric surface Γ is parameterized as

$$\mathbf{X}(\alpha, \varphi) = r(\alpha)\mathbf{e}_r + z(\alpha)\mathbf{e}_z = \begin{pmatrix} r(\alpha) \cos \varphi \\ r(\alpha) \sin \varphi \\ z(\alpha) \end{pmatrix}, \quad \alpha \in [0, 1], \quad \varphi \in [0, 2\pi). \quad (\text{A.1})$$

Given a single-layer density $\mathbf{f}(\alpha, \varphi) = f^r(\alpha)\mathbf{e}_r + f^z(\alpha)\mathbf{e}_z$, we compute the single-layer integral

$$(S[\mathbf{f}])_i(\mathbf{X}) = \int_{\Gamma} G_{ij}(\Delta\mathbf{X})f_j(\mathbf{X}') d\mu_{\Gamma}, \quad \mathbf{X} \in \Gamma, \quad (\text{A.2})$$

where $\Delta\mathbf{X} = \mathbf{X} - \mathbf{X}'$ and G_{ij} is the Stokes-let defined in (2.26). We split the integral into two parts and compute them separately

$$(S[\mathbf{f}])_i(\mathbf{X}) = -\frac{1}{8\pi} \int_{\Gamma} \frac{f_i(\mathbf{X}')}{|\Delta\mathbf{X}|} + \frac{\Delta\mathbf{X} \cdot \mathbf{f}(\mathbf{X}')}{|\Delta\mathbf{X}|^3} (\Delta\mathbf{X})_i d\mu_{\Gamma} := -\frac{1}{8\pi} ((S^{(1)}[\mathbf{f}])_i + (S^{(2)}[\mathbf{f}])_i), \quad (\text{A.3})$$

. First, let us define the function I_{mn} as

$$I_{mn}(r_1, r_2, \hat{z}) = \int_0^{2\pi} \frac{(\cos \varphi')^n}{(r_1^2 + r_2^2 + \hat{z}^2 - 2r_1r_2 \cos \varphi')^{\frac{m}{2}}} d\varphi'. \quad (\text{A.4})$$

We next recast I_{mn} as a linear combination of complete elliptic integrals using Equation (3.19): For the first term $S^{(1)}\mathbf{f}$, we compute the components $-8\pi(S^{(1)}\mathbf{f})_i$ for $i = 1, 2, 3$. The first component is given by

$$\int_{\Gamma} \frac{f_1(\mathbf{X}')}{|\Delta\mathbf{X}|} d\mu_{\Gamma} = \int_0^1 f^r(\alpha')r(\alpha')\sqrt{r_{\alpha}^2(\alpha') + z_{\alpha}^2(\alpha')} \left(\int_0^{2\pi} \frac{\cos \varphi'}{|\Delta\mathbf{X}|} d\varphi' \right) d\alpha'. \quad (\text{A.5})$$

The inner integral can be rewritten as

$$\begin{aligned} \int_0^{2\pi} \frac{\cos \varphi'}{|\Delta \mathbf{X}|} d\varphi' &= \cos \varphi \int_0^{2\pi} \frac{\cos \varphi'}{(r(\alpha)^2 + r(\alpha')^2 + (z(\alpha) - z(\alpha'))^2 - 2r(\alpha)r(\alpha') \cos \varphi')^{\frac{1}{2}}} d\varphi' \\ &= \cos \varphi I_{11}(r(\alpha), r(\alpha'), z(\alpha) - z(\alpha')). \end{aligned} \quad (\text{A.6})$$

Similarly, the second component can be written as

$$\int_{\Gamma} \frac{f_2(\mathbf{X}')}{|\Delta \mathbf{X}|} d\mu_{\Gamma} = \sin \varphi \int_0^1 I_{11}(r(\alpha), r(\alpha'), z(\alpha) - z(\alpha')) f^r(\alpha') r(\alpha') \sqrt{r_{\alpha}^2(\alpha') + z_{\alpha}^2(\alpha')} d\alpha', \quad (\text{A.7})$$

The third component can be written as

$$\int_{\Gamma} \frac{f_3(\mathbf{X}')}{|\Delta \mathbf{X}|} d\mu_{\Gamma} = \int_0^1 I_{10}(r(\alpha), r(\alpha'), z(\alpha) - z(\alpha')) f^r(\alpha') r(\alpha') \sqrt{r_{\alpha}^2(\alpha') + z_{\alpha}^2(\alpha')} d\alpha'. \quad (\text{A.8})$$

Therefore, $S^{(1)}[\mathbf{f}]$ can also be written as an axisymmetric vector-valued function $S^{(1)}[\mathbf{f}] = (S^{(1)}[\mathbf{f}]^r) \mathbf{e}_r + (S^{(1)}[\mathbf{f}]^z) \mathbf{e}_z$ where

$$\begin{pmatrix} (S^{(1)}[\mathbf{f}]^r) \\ (S^{(1)}[\mathbf{f}]^z) \end{pmatrix} = -\frac{1}{8\pi} \int_0^1 \left(S^{(1)}(\alpha, \alpha') \cdot \begin{pmatrix} f^r(\alpha') \\ f^z(\alpha') \end{pmatrix} \right) \sqrt{r_{\alpha}^2(\alpha') + z_{\alpha}^2(\alpha')} d\alpha', \quad (\text{A.9})$$

with the kernel

$$S^{(1)}(\alpha, \alpha') = r(\alpha') \begin{pmatrix} I_{11} & 0 \\ 0 & I_{10} \end{pmatrix}. \quad (\text{A.10})$$

Now, we consider the second term $S^{(2)}\mathbf{f}$. The numerator and denominator of the integrand can be simplified to

$$\Delta \mathbf{X} \cdot \mathbf{f}(\mathbf{X}') = f^r(\alpha') r(\alpha) \cos(\varphi' - \varphi) - f^r(\alpha') r(\alpha') + f^z(\alpha') (z(\alpha) - z(\alpha')), \quad (\text{A.11})$$

and

$$|\Delta \mathbf{X}|^3 = (r(\alpha)^2 + r(\alpha')^2 + (z(\alpha) - z(\alpha'))^2 - 2r(\alpha)r(\alpha') \cos(\varphi' - \varphi))^{\frac{3}{2}} := L_3(\alpha, \alpha', \varphi' - \varphi). \quad (\text{A.12})$$

Then, we have

$$\frac{\Delta \mathbf{X} \cdot \mathbf{f}(\mathbf{X}')}{|\Delta \mathbf{X}|^3} (\Delta \mathbf{X})_1 = \frac{(r(\alpha) \cos \varphi - r(\alpha') \cos \varphi') (f^r(\alpha') r(\alpha) \cos(\varphi' - \varphi) - f^r(\alpha') r(\alpha') + f^z(\alpha') (z(\alpha) - z(\alpha')))}{L_3(\alpha, \alpha', \varphi' - \varphi)}. \quad (\text{A.13})$$

Integrating φ' from 0 to 2π gives

$$\begin{aligned} \int_0^{2\pi} \frac{\Delta \mathbf{X} \cdot \mathbf{f}(\mathbf{X}')}{|\Delta \mathbf{X}|^3} (\Delta \mathbf{X})_1 d\varphi' &= f^r(\alpha') r^2(\alpha) \cos \varphi \int_0^{2\pi} \frac{\cos(\varphi' - \varphi)}{L_3(\alpha, \alpha', \varphi' - \varphi)} d\varphi' \\ &\quad + r(\alpha) \cos \varphi (f^z(\alpha') (z(\alpha) - z(\alpha')) - f^r(\alpha') r(\alpha')) \int_0^{2\pi} \frac{1}{L_3(\alpha, \alpha', \varphi' - \varphi)} d\varphi' \\ &\quad - r(\alpha') r(\alpha) f^r(\alpha') \int_0^{2\pi} \frac{\cos \varphi' \cos(\varphi' - \varphi)}{L_3(\alpha, \alpha', \varphi' - \varphi)} d\varphi' \\ &\quad + r(\alpha') (f^r(\alpha') r(\alpha') - f^z(\alpha') (z(\alpha) - z(\alpha'))) \int_0^{2\pi} \frac{\cos \varphi'}{L_3(\alpha, \alpha', \varphi' - \varphi)} d\varphi'. \end{aligned} \quad (\text{A.14})$$

The integrals inside can be simplified using the function I_{mn} ,

$$\int_0^{2\pi} \frac{\cos(\varphi' - \varphi)}{L_3(\alpha, \alpha', \varphi' - \varphi)} d\varphi' = \int_0^{2\pi} \frac{\cos(\varphi')}{L(\alpha, \alpha', \varphi')} d\varphi' = I_{31}(r(\alpha), r(\alpha'), \Delta z), \quad (\text{A.15})$$

$$\int_0^{2\pi} \frac{1}{L_3(\alpha, \alpha', \varphi' - \varphi)} d\varphi' = I_{30}(r(\alpha), r(\alpha'), \Delta z), \quad (\text{A.16})$$

$$\int_0^{2\pi} \frac{\cos \varphi' \cos(\varphi' - \varphi)}{L_3(\alpha, \alpha', \varphi' - \varphi)} d\varphi' = \cos \varphi I_{32}(r(\alpha), r(\alpha'), \Delta z), \quad (\text{A.17})$$

$$\int_0^{2\pi} \frac{\cos \varphi'}{L_3(\alpha, \alpha', \varphi' - \varphi)} d\varphi' = \cos \varphi I_{31}(r(\alpha), r(\alpha'), \Delta z). \quad (\text{A.18})$$

Then, we obtain

$$\int_0^{2\pi} \frac{\Delta \mathbf{X} \cdot \mathbf{f}(\mathbf{X}')}{|\Delta \mathbf{X}|^3} (\Delta \mathbf{X})_1 d\varphi' = \{((r^2(\alpha) + r^2(\alpha'))I_{31} - r(\alpha)r(\alpha')(I_{30} + I_{32})) f^r(\alpha') \quad (\text{A.19})$$

$$+ ((r(\alpha)I_{30} - r(\alpha')I_{31})(z(\alpha) - z(\alpha')f^z(\alpha'))\} \cos \varphi. \quad (\text{A.20})$$

Hence, the first component of $S^{(2)}\mathbf{f}$ is given by

$$\begin{aligned} \int_{\Gamma} \frac{\Delta \mathbf{X} \cdot \mathbf{f}(\mathbf{X}')}{|\Delta \mathbf{X}|^3} (\Delta \mathbf{X})_1 d\mu_{\Gamma} &= \int_0^1 r(\alpha') \sqrt{r_{\alpha}^2(\alpha') + z_{\alpha}^2(\alpha')} \int_0^{2\pi} \frac{\Delta \mathbf{X} \cdot \mathbf{f}(\mathbf{X}')}{|\Delta \mathbf{X}|^3} (\Delta \mathbf{X})_1 d\varphi' d\alpha' \\ &= \cos \varphi \int_0^1 r(\alpha') \sqrt{r_{\alpha}^2(\alpha') + z_{\alpha}^2(\alpha')} \left((S_{11}^{(2)}, S_{12}^{(2)}) (\alpha, \alpha') \cdot \begin{pmatrix} f^r(\alpha') \\ f^z(\alpha') \end{pmatrix} \right) d\alpha', \end{aligned} \quad (\text{A.21})$$

where the kernel is given by

$$(S_{11}^{(2)}, S_{12}^{(2)}) (\alpha, \alpha') = ((r^2 + (r')^2)I_{31} - rr'(I_{30} + I_{32}), \quad \Delta z(rI_{30} - r'I_{31})), \quad (\text{A.22})$$

Similarly, the second component of $S^{(2)}\mathbf{f}$ is given by

$$\int_{\Gamma} \frac{\Delta \mathbf{X} \cdot \mathbf{f}(\mathbf{X}')}{|\Delta \mathbf{X}|^3} (\Delta \mathbf{X})_2 d\mu_{\Gamma} = \sin \varphi \int_0^1 r(\alpha') \sqrt{r_{\alpha}^2(\alpha') + z_{\alpha}^2(\alpha')} \left((S_{11}^{(2)}, S_{12}^{(2)}) (\alpha, \alpha') \cdot \begin{pmatrix} f^r(\alpha') \\ f^z(\alpha') \end{pmatrix} \right) d\alpha'. \quad (\text{A.23})$$

For the third component, we first compute

$$\frac{\Delta \mathbf{X} \cdot \mathbf{f}(\mathbf{X}')}{|\Delta \mathbf{X}|^3} (\Delta \mathbf{X})_3 = \frac{(z(\alpha) - z(\alpha'))(f^r(\alpha')r(\alpha) \cos(\varphi' - \varphi) - f^r(\alpha')r(\alpha') + f^z(\alpha')(z(\alpha) - z(\alpha')))}{L_3(\alpha, \alpha', \varphi' - \varphi)}. \quad (\text{A.24})$$

Integrating φ' from 0 to 2π , we have

$$\int_0^{2\pi} \frac{\Delta \mathbf{X} \cdot \mathbf{f}(\mathbf{X}')}{|\Delta \mathbf{X}|^3} (\Delta \mathbf{X})_3 d\varphi' = (\Delta z(rI_{31} - r'I_{30})f^r(\alpha') + (\Delta z)^2 I_{30}f^z(\alpha')). \quad (\text{A.25})$$

The third component of $S^{(2)}\mathbf{f}$ is given by

$$\int_{\Gamma} \frac{\Delta \mathbf{X} \cdot \mathbf{f}(\mathbf{X}')}{|\Delta \mathbf{X}|^3} (\Delta \mathbf{X})_3 d\mu_{\Gamma} = \int_0^1 r(\alpha') \sqrt{r_{\alpha}^2(\alpha') + z_{\alpha}^2(\alpha')} \int_0^{2\pi} \frac{\Delta \mathbf{X} \cdot \mathbf{f}(\mathbf{X}')}{|\Delta \mathbf{X}|^3} (\Delta \mathbf{X})_3 d\varphi' d\alpha' \quad (\text{A.26})$$

$$= \int_0^1 r(\alpha') \sqrt{r_{\alpha}^2(\alpha') + z_{\alpha}^2(\alpha')} \left((S_{21}^{(2)}, S_{22}^{(2)}) (\alpha, \alpha') \cdot \begin{pmatrix} f^r(\alpha') \\ f^z(\alpha') \end{pmatrix} \right) d\alpha' \quad (\text{A.27})$$

where the kernel vector is given by

$$(S_{21}^{(2)}, S_{22}^{(2)}) (\alpha, \alpha') = (\Delta z(rI_{31} - r'I_{30}), \quad (\Delta z)^2 I_{30}), \quad (\text{A.28})$$

Summarizing the computation above, we have $S[\mathbf{f}] = (S[\mathbf{f}]^r e_r + (S[\mathbf{f}]^z e_z$ where

$$\begin{pmatrix} (S[\mathbf{f}]^r)^r \\ (S[\mathbf{f}]^z)^z \end{pmatrix} = -\frac{1}{8\pi} \int_0^1 r(\alpha') \left(\mathcal{S}(\alpha, \alpha') \cdot \begin{pmatrix} f^r(\alpha') \\ f^z(\alpha') \end{pmatrix} \right) \sqrt{r_{\alpha}^2(\alpha') + z_{\alpha}^2(\alpha')} d\alpha', \quad (\text{A.29})$$

with the kernel

$$\mathcal{S}(\alpha, \alpha') = \begin{pmatrix} I_{11} + (r^2 + (r')^2)I_{31} - rr'(I_{30} + I_{32}) & \Delta z(rI_{30} - r'I_{31}) \\ \Delta z(rI_{31} - r'I_{30}) & I_{10} + (\Delta z)^2 I_{30} \end{pmatrix}. \quad (\text{A.30})$$

Setting α as the arc-length parameter of the generating curve, we can obtain (3.17) and (3.18).

B. Analytical solution for a planar membrane

Consider an annular-shaped planar membrane which is defined by (5.5). The governing equation (2.24) simplifies to the equations as follows,

$$-\partial_r p + \mu (\mathcal{L}_1[u^r] + \partial_{zz}u^r) = 0, \text{ in } \Omega, \quad (\text{B.1a})$$

$$-\partial_z p + \mu (\mathcal{L}_0[u^z] + \partial_{zz}u^z) = 0, \text{ in } \Omega, \quad (\text{B.1b})$$

$$\frac{1}{r}\partial_r(ru^r) + \partial_z u^z = 0, \text{ in } \Omega, \quad (\text{B.1c})$$

$$-\partial_r P + \mu_\Gamma \mathcal{L}_1[U] - \llbracket \mu \partial_z u^r \rrbracket = 0, \text{ in } \Gamma, \quad (\text{B.1d})$$

$$\frac{1}{r}\partial_r(rU) = 0, \text{ in } \Gamma, \quad (\text{B.1e})$$

$$-P + 2\mu_\Gamma \partial_r U + \frac{\gamma}{R_o} = 0, \text{ on } \{z = 0, r = R_o\}, \quad (\text{B.1f})$$

$$-P + 2\mu_\Gamma \partial_r U - \frac{\gamma}{R_i} = 0, \text{ on } \{z = 0, r = R_i\}, \quad (\text{B.1g})$$

$$u^r = U, \text{ in } \Gamma, \quad (\text{B.1h})$$

$$\partial_i R_k = U(R_k), k = i, o, \text{ in } \Gamma, \quad (\text{B.1i})$$

where $U = U^r$ is the radial velocity of the membrane and \mathcal{L}_ν is the differential operator defined as

$$\mathcal{L}_\nu = \partial_{rr} + \frac{1}{r}\partial_r - \frac{\nu^2}{r^2}, \quad \nu = 0, 1. \quad (\text{B.2})$$

From the inextensibility condition (B.1e), we obtain

$$U = \frac{F}{r}, \quad r \in [R_i, R_o], \quad (\text{B.3})$$

where F is spatially constant. In the limit of $R_o \rightarrow \infty$, following the same technique used in [58], we can obtain the surface tension we have

$$P(r) = \frac{4\mu F}{R_i} \sin^{-1}\left(\frac{R_i}{r}\right), \quad r > R_i. \quad (\text{B.4})$$

Plugging (B.4) into the following stress balance equation at the open edge,

$$-P_i^+ - 2\mu_\Gamma \frac{F}{R_i^2} - \frac{\gamma}{R_i} = 0, \quad (\text{B.5})$$

where P_i^+ is the limiting value of $P(r)$ at $r = R_i$ from the side of the membrane, we can obtain the expression for the constant F ,

$$F = -\frac{\gamma R_i}{2(\pi\mu R_i + \mu_\Gamma)} = -\frac{\gamma}{2\pi\mu} \left(1 + \frac{\mu_\Gamma}{\pi\mu R_i}\right)^{-1}. \quad (\text{B.6})$$

The above computation also gives the derivative of the surface tension, revealing the singularity of the single-layer density ξ as $r \rightarrow R_i^+$,

$$\frac{dP}{dr} = -\frac{4\mu F}{r\sqrt{r^2 - R_i^2}}, \quad \xi = -\frac{dP}{dr} e_r. \quad (\text{B.7})$$

C. Derivation of a simplified spherical cap model

Suppose the membrane is always a spherical cap obtained by rotating the generating curve

$$C = \{(R \sin(\theta), z_0 + R \cos(\theta)), 0 \leq \theta \leq \alpha\}, \quad (\text{C.1})$$

with $\alpha \in (0, \pi)$ and $R > 0$. The shape is described by three parameters R, α , and z_0 . Assuming the membrane is rim-less, its velocity is given by [46],

$$\mathbf{U} = U_1 \mathbf{i}_r + U_2 \frac{\tan(\theta/2)}{\tan(\alpha/2)} \mathbf{i}_\theta + U_3 \mathbf{i}_z. \quad (\text{C.2})$$

where $\mathbf{i}_r, \mathbf{i}_\theta, \mathbf{i}_z$ are the unit basis for spherical coordinates and U_1, U_2, U_3 are defined as

$$U_1 = \frac{dR}{dt}, \quad U_2 = R \frac{d\alpha}{dt}, \quad U_3 = \frac{dz_0}{dt}. \quad (\text{C.3})$$

Then, the surface divergence of the velocity is a constant over θ , which is given by

$$\nabla_\Gamma \cdot \mathbf{U} = \frac{1}{R} \left(2U_1 + \cot \frac{\alpha}{2} U_2 \right). \quad (\text{C.4})$$

We consider the following bending energy for the membrane, which includes the Willmore energy and line tension

$$W = 2\pi\alpha (1 - \cos \alpha) + 2\pi\gamma R \sin \alpha. \quad (\text{C.5})$$

Define the Rayleigh dissipation function for the membrane viscosity as

$$\mathcal{E}_\Gamma = \mu_\Gamma \int_\Gamma \mathbf{D}_\Gamma \cdot \mathbf{D}_\Gamma d\mu_\Gamma. \quad (\text{C.6})$$

To enforce the local inextensibility constraint, we form a Lagrange functional by

$$L_\Gamma = \mathcal{E}_\Gamma - \int_\Gamma P (\nabla_\Gamma \cdot \mathbf{U}) d\mu_\Gamma, \quad (\text{C.7})$$

where P is the effective surface tension acting like a Lagrangian multiplier. Since $\nabla_\Gamma \cdot \mathbf{U}$ is independent of θ , suggesting that imposing the local inextensibility constraint is equivalent to imposing the following constraint of a single algebraic equation

$$\frac{1}{R} \left(2U_1 + \cot \frac{\alpha}{2} U_2 \right) = 0. \quad (\text{C.8})$$

Thus, the Lagrange functional can be written as

$$L_\Gamma = \mathcal{E}_\Gamma - \bar{P} A \frac{1}{R} \left(2U_1 + \cot \frac{\alpha}{2} U_2 \right), \quad (\text{C.9})$$

where the averaged surface tension \bar{P} is the effective Lagrangian multiplier. This suggests that under the spherical cap assumption, only the average of the surface tension can be determined by the local inextensibility rather than the surface tension at every point on the membrane. This may be a flaw due to the simplification of the model.

By the principle of maximum dissipation, we obtain the following force balance,

$$F_1 + F_1^s = -\partial_R W, \quad (\text{C.10a})$$

$$F_2 + F_2^s = -R^{-1} \partial_\alpha W, \quad (\text{C.10b})$$

$$F_3 + F_3^s = -\partial_{z_0} W, \quad (\text{C.10c})$$

where $F_i^s = \partial_{U_i} L_\Gamma$ are membrane viscosity forces given by

$$\begin{aligned} F_1^s &= 2\pi\mu_\Gamma (\cos(\alpha) - 1) \left(8U_1 + 4U_2 \cot \left(\frac{\alpha}{2} \right) \right) \\ &\quad - 2\pi\mu_\Gamma (2U_1 (6 \cos(\alpha) - 6) - 6U_2 \sin(\alpha)) + 2\pi P R (\cos(\alpha) - 1), \\ F_2^s &= 2\pi\mu_\Gamma \left(6U_1 \sin(\alpha) - 2U_2 \left((2 \cos(\alpha) + 2) \left(\frac{2 \log \left(\cos \left(\frac{\alpha}{2} \right) \right)}{\cos(\alpha) - 1} - 1 \right) - 1 \right) \right) \end{aligned} \quad (\text{C.11})$$

$$+ 4\pi\mu\Gamma \cot\left(\frac{\alpha}{2}\right)(\cos(\alpha) - 1)\left(2U_1 + U_2 \cot\left(\frac{\alpha}{2}\right)\right) + \pi PR \cot\left(\frac{\alpha}{2}\right)(\cos(\alpha) - 1), \quad (\text{C.12})$$

$$F_3^s = 0, \quad (\text{C.13})$$

and F_i are forces exerted on the fluid computed in [46], given by

$$F_1 = -4\pi R^2 (\Delta p^{(1)} + \Delta p^{(2)} + \Delta p^{(3)}), \quad (\text{C.14})$$

$$F_2 = \mu R \cot\left(\frac{\alpha}{2}\right) \left((\alpha - \sin\alpha + \alpha^2 \tan\left(\frac{\alpha}{2}\right)) \left(12U_1 + 8 \cot\left(\frac{\alpha}{2}\right)U_2\right) + (\sin 2\alpha + 4\alpha \cos\alpha - 2\alpha - 4 \sin\alpha)U_3 \right), \quad (\text{C.15})$$

$$F_3 = \mu R \left[(6\alpha + 8 \sin\alpha + \sin 2\alpha)(U_1 + U_3) + \cot\left(\frac{\alpha}{2}\right)(\sin 2\alpha + 4\alpha \cos\alpha - 2\alpha - 4 \sin\alpha)U_2 \right] = 0. \quad (\text{C.16})$$

with

$$\Delta p^{(1)} = \frac{1}{\pi^2} \left[(1 - 2 \cos\alpha) \sin^2\alpha + \frac{1}{2}\alpha(11 - \cos\alpha) \sin\alpha + 3\alpha^2(2 + \cos\alpha) \sin^2\left(\frac{\alpha}{2}\right) \right] \frac{\mu q}{c^3}, \quad (\text{C.17})$$

$$\Delta p^{(2)} = -12 \cot\left(\frac{\alpha}{2}\right) \left(\alpha - \sin\alpha + \alpha^2 \tan\left(\frac{\alpha}{2}\right) \right) \frac{\mu U_2}{4\pi R}, \quad (\text{C.18})$$

$$\Delta p^{(3)} = -(6\alpha + 8 \sin\alpha + \sin 2\alpha) \frac{\mu U_3}{4\pi R}, \quad (\text{C.19})$$

and $c = R \sin\alpha$ is the radius of the pore. The force balance equations (C.10) together with the inextensibility constraint (C.8) form four linear equations for U_1, U_2, U_3, P . Solving the equations gives the expression of U_1, U_2, U_3, P in terms of R, α, z_0 ,

$$U_1 = U_1(R, \alpha, z_0), \quad (\text{C.20a})$$

$$U_2 = U_2(R, \alpha, z_0), \quad (\text{C.20b})$$

$$U_3 = U_3(R, \alpha, z_0), \quad (\text{C.20c})$$

$$P = P(R, \alpha, z_0). \quad (\text{C.20d})$$

Combined with the geometric evolution equation (C.3), we obtain an ODE system that describes the dynamics of the spherical cap,

$$\frac{dR}{dt} = U_1 = f_R(R, \alpha), \quad (\text{C.21a})$$

$$\frac{d\alpha}{dt} = R^{-1}U_2 = f_\alpha(R, \alpha) \quad (\text{C.21b})$$

$$\frac{dz_0}{t} = U_3 = f_{z_0}(R, \alpha), \quad (\text{C.21c})$$

$$P = P(R, \alpha). \quad (\text{C.21d})$$

Note that the equation for z_0 is decoupled from the one for R and α and P only depends on the geometry. We can further reduce the equations into a single equation for R or α . We have used MATLAB's symbolic computation toolbox for the derivation of the equations, and the resulting ODE system is numerically integrated using the `ode45` solver.

Acknowledgements

YM was partially supported by the National Science Foundation (NSF) grant DMR2309034 (USA), and the Math+X award from the Simons Foundation (Award ID 234606). YNY acknowledges support from the NSF under Award No. DMS-1951600, and from the Flatiron Institute, part of Simons Foundation.

References

- [1] A. Saitoh, K. Takiguchi, Y. Tanaka, H. Hotani, Opening-up of liposomal membranes by talin, *Proceedings of the National Academy of Sciences* 95 (1998) 1026–1031.

- [2] C. Misbah, Vacillating breathing and tumbling of vesicles under shear flow, *Physical Review Letters* 96 (2006) 028104.
- [3] S. T. Cooper, P. L. McNeil, Membrane repair: Mechanisms and pathophysiology, *Physiological Reviews* 95 (2015) 1205–1240.
- [4] M. Arroyo, A. Desimone, Relaxation dynamics of fluid membranes, *Physical Review E - Statistical, Nonlinear, and Soft Matter Physics* 79 (2009) 1–17.
- [5] C. A. Aubin, R. J. Ryham, Stokes flow for a shrinking pore, *Journal of Fluid Mechanics* 788 (2016) 228–245.
- [6] M. C. Lai, Z. Li, A remark on jump conditions for the three-dimensional navier-stokes equations involving an immersed moving membrane, *Applied Mathematics Letters* 14 (2001) 149–154.
- [7] R. Cortez, C. S. Peskin, J. M. Stockie, D. Varela, Parametric resonance in immersed elastic boundaries, *SIAM Journal on Applied Mathematics* 65 (2005) 494–520.
- [8] U. Seifert, Configurations of fluid membranes and vesicles, *Advances in physics* 46 (1997) 13–137.
- [9] A. Biria, M. Maleki, E. Fried, *Continuum Theory for the Edge of an Open Lipid Bilayer*, volume 46, 1 ed., Elsevier Inc., 2013, pp. 1–68. URL: <http://dx.doi.org/10.1016/B978-0-12-396522-6.00001-3> <https://linkinghub.elsevier.com/retrieve/pii/B9780123965226000013>. doi:10.1016/B978-0-12-396522-6.00001-3.
- [10] F. Jülicher, U. Seifert, Shape equations for axisymmetric vesicles: A clarification, *Physical Review E* 49 (1994) 4728–4731.
- [11] D. Steigmann, E. Baesu, R. E. Rudd, J. Belak, M. McElfresh, On the variational theory of cell-membrane equilibria, *Interfaces and Free Boundaries* 5 (2003) 357–366.
- [12] Y. Kim, M.-c. Lai, Simulating the dynamics of inextensible vesicles by the penalty immersed boundary method, *Journal of Computational Physics* 229 (2010) 4840–4853.
- [13] M. C. Lai, K. C. Ong, Unconditionally energy stable schemes for the inextensible interface problem with bending, *SIAM Journal on Scientific Computing* 41 (2019) B649–B668.
- [14] K. Chuan, M.-c. Lai, Y. Seol, An immersed boundary projection method for incompressible interface simulations in 3D flows, *Journal of Computational Physics* 430 (2021) 110090.
- [15] M. C. Lai, Y. Seol, A stable and accurate immersed boundary method for simulating vesicle dynamics via spherical harmonics, *Journal of Computational Physics* 449 (2022) 110785.
- [16] S. K. Veerapaneni, D. Gueyffier, G. Biros, D. Zorin, A numerical method for simulating the dynamics of 3D axisymmetric vesicles suspended in viscous flows, *Journal of Computational Physics* 228 (2009) 7233–7249.
- [17] A. Farutin, T. Biben, C. Misbah, 3D numerical simulations of vesicle and inextensible capsule dynamics, *Journal of Computational Physics* 275 (2014) 539–568.
- [18] S. H. Hsu, J. Chu, M. C. Lai, R. Tsai, A coupled grid based particle and implicit boundary integral method for two-phase flows with insoluble surfactant, *Journal of Computational Physics* 395 (2019) 747–764.
- [19] J. W. Barrett, H. Garcke, R. Nürnberg, Parametric finite element approximations of curvature-driven interface evolutions, in: *Handbook of Numerical Analysis*, volume 21, 2020, pp. 275–423. URL: <https://linkinghub.elsevier.com/retrieve/pii/S1570865919300055>. doi:10.1016/bs.hna.2019.05.002. arXiv:1903.09462.
- [20] M. Bottacchiari, M. Gallo, M. Bussoletti, C. M. Casciola, The diffuse interface description of fluid lipid membranes captures key features of the hemifusion pathway and lateral stress profile, *PNAS Nexus* 3 (2024) 1–10.
- [21] S. Reuther, A. Voigt, Incompressible two-phase flows with an inextensible Newtonian fluid interface, *Journal of Computational Physics* 322 (2016) 850–858.
- [22] W.-F. Hu, M.-C. Lai, Y.-N. Young, A hybrid immersed boundary and immersed interface method for electrohydrodynamic simulations, *Journal of Computational Physics* 282 (2015) 47–61.
- [23] W.-F. Hu, M.-C. Lai, Y. Seol, Y.-N. Young, Vesicle electrohydrodynamic simulations by coupling immersed boundary and immersed interface method, *Journal of Computational Physics* 317 (2016) 66–81.
- [24] R. Ryham, I. Berezovik, F. S. Cohen, Aqueous viscosity is the primary source of friction in lipidic pore dynamics, *Biophysical Journal* 101 (2011) 2929–2938.
- [25] S. K. Y. Tang, W. F. Marshall, Self-repairing cells: How single cells heal membrane ruptures and restore lost structures, *Science* 356 (2017) 1022–1025.
- [26] M. B. Klenow, M. S. Vigsø, W. Pezeshkian, J. Nylandsted, M. A. Lomholt, A. C. Simonsen, Shape of the membrane neck around a hole during plasma membrane repair, *Biophysical Journal* 123 (2024) 1827–1837.
- [27] V. K. Malik, O. S. Pak, J. Feng, Pore dynamics of lipid vesicles under light-induced osmotic stress, *Physical Review Applied* 17 (2022) 1.
- [28] N. Srividya, S. Muralidharan, Determination of the line tension of giant vesicles from pore-closing dynamics, *The Journal of Physical Chemistry B* 112 (2008) 7147–7152.
- [29] T. Umeda, Y. Suezaki, K. Takiguchi, H. Hotani, Theoretical analysis of opening-up vesicles with single and two holes, *Physical Review E* 71 (2005) 011913.
- [30] R. J. Ryham, M. A. Ward, F. S. Cohen, Teardrop shapes minimize bending energy of fusion pores connecting planar bilayers, *Physical Review E—Statistical, Nonlinear, and Soft Matter Physics* 88 (2013) 062701.
- [31] S.-P. P. Fu, R. Ryham, A. Klöckner, M. Wala, S. Jiang, Y.-N. Young, Simulation of multiscale hydrophobic lipid dynamics via efficient integral equation methods, *Multiscale Modeling & Simulation* 18 (2020) 79–103.
- [32] M. Asgari, A. Biria, Free energy of the edge of an open lipid bilayer based on the interactions of its constituent molecules, *International Journal of Non-Linear Mechanics* 76 (2015) 135–143.
- [33] J. C. Alexander, A. J. Bernoff, E. K. Mann, J. A. Mann, L. Zou, Hole dynamics in polymer langmuir films, *Physics of Fluids* 18 (2006).
- [34] A. Laadhari, C. Misbah, P. Saramito, On the equilibrium equation for a generalized biological membrane energy by using a shape optimization approach, *Physica D* 239 (2010) 1567–1572.
- [35] R. Capovilla, J. Guven, J. A. Santiago, Lipid membranes with an edge, *Physical Review E - Statistical Physics, Plasmas, Fluids, and Related Interdisciplinary Topics* 66 (2002) 1–7.

- [36] M. Deserno, Fluid lipid membranes: From differential geometry to curvature stresses, *Chemistry and Physics of Lipids* 185 (2015) 11–45.
- [37] B. Palmer, Álvaro Pámpano, Minimizing configurations for elastic surface energies with elastic boundaries, *Journal of Nonlinear Science* 31 (2021) 23.
- [38] B. Palmer, Álvaro Pámpano, The euler–helfrich functional, *Calculus of Variations and Partial Differential Equations* 61 (2022) 1–28.
- [39] Z. C. Tu, Compatibility between shape equation and boundary conditions of lipid membranes with free edges, *The Journal of Chemical Physics* 132 (2010).
- [40] Z. Tu, Geometry of membranes, *Journal of Geometry and Symmetry in Physics* 24 (2011) 45–75.
- [41] B. Palmer, Álvaro Pámpano, Symmetry breaking bifurcation of membranes with boundary, *Nonlinear Analysis, Theory, Methods and Applications* 238 (2024) 113393.
- [42] Z. C. Tu, Z. C. Ou-Yang, Lipid membranes with free edges, *Physical Review E - Statistical Physics, Plasmas, Fluids, and Related Interdisciplinary Topics* 68 (2003) 1–7.
- [43] X. Zhou, An integral case of the axisymmetric shape equation of open vesicles with free edges, *International Journal of Non-Linear Mechanics* 106 (2018) 25–28.
- [44] Y. Yin, J. Yin, D. Ni, General mathematical frame for open or closed biomembranes (part i): Equilibrium theory and geometrically constraint equation, *Journal of Mathematical Biology* 51 (2005) 403–413.
- [45] Y. Yin, Y. Chen, D. Ni, H. Shi, Q. Fan, Shape equations and curvature bifurcations induced by inhomogeneous rigidities in cell membranes, *Journal of Biomechanics* 38 (2005) 1433–1440.
- [46] R. J. Ryham, On the viscous flows of leak-out and spherical cap natation, *Journal of Fluid Mechanics* 836 (2018) 502–531.
- [47] F. S. Cohen, R. Eisenberg, R. J. Ryham, A dynamic model of open vesicles in fluids, *Communications in Mathematical Sciences* 10 (2012) 1273–1285.
- [48] F. S. Cohen, R. J. Ryham, The aqueous viscous drag of a contracting open surface, *Physics of Fluids* 26 (2014).
- [49] X. Wang, Q. Du, Modelling and simulations of multi-component lipid membranes and open membranes via diffuse interface approaches, *Journal of Mathematical Biology* 56 (2007) 347–371.
- [50] J. W. Barrett, H. Garcke, R. Nürnberg, Stable variational approximations of boundary value problems for willmore flow with gaussian curvature, *IMA Journal of Numerical Analysis* 37 (2017) 1657–1709.
- [51] J. W. Barrett, H. Garcke, R. Nürnberg, Stable approximations for axisymmetric willmore flow for closed and open surfaces, *ESAIM: Mathematical Modelling and Numerical Analysis* 55 (2021) 833–885.
- [52] Y. Hayashi, Three-dimensional dirichlet problem for the helmholtz equation for an open boundary, *Proceedings of the Japan Academy, Series A, Mathematical Sciences* 53 (1977) 1–23.
- [53] V. Kirvalidze, The dirichlet problem for stokes equation in a domain exterior to an open surface, *Mathematical Methods in the Applied Sciences* 20 (1997) 1257–1269.
- [54] E. P. Stephan, Boundary integral equations for screen problems in ir³, *Integral Equations and Operator Theory* 10 (1987) 236–257.
- [55] S. Jiang, V. Rokhlin, Second kind integral equations for the classical potential theory on open surfaces ii, *Journal of Computational Physics* 195 (2004) 1–16.
- [56] S. Jiang, V. Rokhlin, Second kind integral equations for the classical potential theory on open surfaces i: Analytical apparatus, *Journal of Computational Physics* 191 (2003) 40–74.
- [57] J. Helsing, S. Jiang, The helmholtz dirichlet and neumann problems on piecewise smooth open curves, 2024. URL: <https://arxiv.org/abs/2411.05761>. arXiv:2411.05761.
- [58] L. L. Jia, M. J. Shelley, The role of monolayer viscosity in Langmuir film hole closure dynamics, *Journal of Fluid Mechanics* 948 (2022) A1.
- [59] Y. Hyon, D. Y. Kwak, C. Liu, Energetic variational approach in complex fluids: maximum dissipation principle, *Discrete Contin. Dyn. Syst* 26 (2010) 1291–1304.
- [60] G. Guennebaud, B. Jacob, et al., Eigen: A C++ template library for linear algebra, 2010. URL: <http://eigen.tuxfamily.org>.
- [61] B. K. Alpert, Hybrid Gauss-Trapezoidal Quadrature Rules, *SIAM Journal on Scientific Computing* 20 (1999) 1551–1584.
- [62] T. R. Powers, G. Huber, R. E. Goldstein, Fluid-membrane tethers: Minimal surfaces and elastic boundary layers, *Physical Review E - Statistical Physics, Plasmas, Fluids, and Related Interdisciplinary Topics* 65 (2002) 11.
- [63] S.-P. Fu, B. Quaife, R. Ryham, Y.-N. Young, Two-dimensional hydrodynamics of a janus particle vesicle, *Journal of Fluid Mechanics* 941 (2022) A41.